Discontinuous Galerkin formulation for 2D hydrodynamic modelling: Trade-offs between theoretical complexity and practical convenience

Georges Kesserwani*, Janice Lynn Ayog, Domenico Bau

Department of Civil and Structural Engineering, Mappin Building, S1 3JD University of Sheffield, Sheffield, UK

Highlights

- Second-order Discontinuous Galerkin (DG2) models on quadrilateral elements for modelling 2D hydrodynamics.
- Standard 2D-DG2 form simplified to a so-called "slope-decoupled" form for robustness and efficiency purposes.
- Well-balancedness of the slope-decoupled 2D-DG2 planar solutions is theoretically studied.
- Both the standard and the slope-decoupled 2D-DG2 schemes deliver comparable accuracy for analytical tests.
- The slope-decoupled 2D-DG2 scheme has attractive conservation properties for developing robust flood models.

Abstract

In the modelling of hydrodynamics, the Discontinuous Galerkin (DG) approach constitutes a more complex and modern alternative to the well-established finite volume method. The latter retains some desired practical features for modelling hydrodynamics, such as well-balancing between spatial flux and steep topography gradients, ability to incorporate wetting and drying processes, and computational affordability. In this context, DG methods were originally devised to solve the two-dimensional (2D) Shallow Water Equations (SWE) with irregular topographies and wetting and drying, albeit at reduction in the formulation's complexity to often being second-order accurate (DG2). The aims of this paper are: (a) to outline a so-called "slope-decoupled" formulation of a standard 2D-DG2-SWE simulator in which theoretical complexity is deliberately reduced; (b) to highlight the capabilities of the proposed slope-decoupled simulator in providing a setting where the simplifying assumptions are verified within the formulation. Both the standard and the slope-decoupled 2D-DG2-SWE models adopt 2D modal basis functions for shaping local planar DG2 solutions on quadrilateral elements, by using an average coefficient and two slope coefficients along the Cartesian coordinates. Over a quadrilateral element, the stencil of the slope-decoupled 2D-DG2 formulation is simplified to remove the interdependence of slope-coefficients for both flow and topography approximations. The fully well-balanced character the slope-decoupled 2D-DG2-SWE planar solutions is theoretically studied. The performance of the latter is compared with the standard 2D-DG2 formulation in classical simulation tests. Other tests are conducted to diagnostically verify the conservative properties of the 2D-DG2-SWE method in scenarios involving sharp topography gradients and wet and/or dry zones. The analyses

---

* Corresponding author.
  E-mail addresses: g.kesserwani@sheffield.ac.uk (G. Kesserwani), jlayog1@sheffield.ac.uk (J.L. Ayog), d.bau@sheffield.ac.uk (D. Bau).

conducted offer strong evidence that the proposed slope-decoupled 2D-DG2-SWE simulator is very attractive for the development of robust flood models.

1. Introduction

Recent literature reviews [1–6] have highlighted that Discontinuous Galerkin (DG) methods have great potential for the formulation of modern numerical models in engineering and physics disciplines. A DG approach elegantly combines the locally-conservative finite volume principle, in the Godunov-type [7–11] sense, with the flexibility of the finite element weak formulation to shape a solution of arbitrary order-of-accuracy over a mesh element [12]. These features allow to attain local high-order approximate solutions, while only needing to communicate with adjacent neighbours for numerical flux calculation, e.g. when explicit Runge–Kutta (RK) time stepping schemes are adopted. This makes the DG method ideal for parallel efficiency on both traditional parallel platforms [13–17] and graphics-processing units (GPUs) [18–21], and fundamental for local h (mesh), p (polynomial order) and t (time step) adaptation and enrichment methodologies [16,17,22–32]. The DG method is also characterised by a local discrete (element-wise) translation of the conservative model equation(s), which is a desired property in multi-physics applications, e.g. in coupling various model components involved in water resources systems [5,33–36]. Compared to other popular alternatives, such as the continuous Galerkin and the finite volume methods, the DG method entails significantly larger computational costs in terms of degrees of freedom (or coefficients) per mesh element. Perhaps, a fairer comparison is to fix a prescribed level of accuracy and/or of conservativeness *vs.* runtime cost and mesh-size required, where DG methods outrival [37–43]. With DG methods, the number of coefficients needed are proportional to the desired order-of-accuracy, the spatial dimensionality involved and the number of equations forming the physical model in question, all of which define the complexity, both theoretical and computational, involved in a DG formulation. In real-world applications, however, compromises on the level of complexity in DG formulations seem to be inevitable and context-specific in favour of model affordability and robustness.

In the modelling of hydrodynamics associated with solving the Shallow Water Equations (SWE) with topography gradients, higher than second-order accurate DG formulations (DG2) are particularly hard to stabilise for ensuring robustness in realistic simulations, owing to a number of persistent and intertwined issues. On one side, the *slope-limiting process*, although crucial to bound the variation of high-order (slope) coefficients around sharp solution gradients, remains unsettled per se (e.g. regarding its localisation, deparametrisation and/or hierarchisation for higher than DG2 solution [44–53]), and may cause adverse effects in the modelling of hydrodynamic flow and transport [43,54–61]. On another, the numerical integration of steep topography gradients is not entirely resolved [62,63], in particular when it comes to ensuring well-balanced numerical predictions [64] for flow scenarios involving terrain shapes that are non-differentiable and/or partially-wet, such as when a local 2D-DG2 planar solution cuts through a dry building-like terrain (see 1D example in [63]). Previous work in this direction primarily considered formulating DG2 schemes on triangular meshes based on nodal basis functions [64–68]. In these works, measures (i.e. extending earlier developments in robust SWE finite volume solvers [69–71]) have often been incorporated to ensuring mass-conservative schemes when modelling the 2D-SWE over uneven topographies with wetting and drying, many of which hinted at the need of further improvements to better preserve second-order accuracy and momentum conservation (e.g. [64,65]). This paper addresses, in part, such need based on reducing the complexity of a modal 2D DG2 formulation on quadrilateral meshes, and supported by theoretical and numerical investigations on its overall well-balanced and conservative properties.

Compared to the triangular mesh type, fewer developments considered quadrilateral meshes in the formulation of robust 2D-DG2-SWE solvers [32,72,73], though comparative studies [74,75] particularly report benefits in both accuracy and efficiency from adopting the quadrilateral mesh setting with DG2 models. It may also be worth noting that this setting is extremely suitable for devising a multiscale 2D-DG solver, e.g. via multiwavelet enrichment functions to the 2D modal bases in which the use of the *same filters* to transfer modelling data across length-scales is crucial to preserve the conservative character of the reference DG scheme [30,31,63]. Existing modal 2D-DG2-SWE

solvers on quadrilateral meshes [30,41,73] have *somehow* explored the well-balancedness property with wetting and drying, *mainly considering the means (or average coefficients) involved in the local DG2 solutions.* These solvers, however, still lack a thorough diagnostic exploration of the full extent of well-balancedness beyond the means and/or differentiable topography shapes. In addition, most previous investigations [30,41,73] employed the pre-balanced SWE [76] in which the free-surface elevation constitutes the main variable, instead of the water height, on the basis of adding extra topography components in flux terms. Compared to the conventional form of the SWE [76], the use of the pre-balanced SWE equations seems to be unnecessary and add to operational costs [76].

To this end, this paper aims to devise a new 2D-DG2-SWE solver based on the conventional form of the SWE, and with in-depth analyses of its well-balanced behaviour for *all the coefficients* defining local planar DG2 solutions (i.e. both *means and slopes*). In Section 2.1, the proposed 2D-DG2 formulation is presented starting with a *standard formulation*. In Section 2.2, such formulation is *purposely* simplified to produce the *slope-decoupled formulation*, where it is further supported with the ability to *fully (i.e. for all coefficients)* preserve the well-balanced property for a range of realistic scenarios. In Section 3, carefully designed test cases are employed to, first, compare the performance of the slope-decoupled 2D-DG2-SWE solver *vs.* the standard version and, next, further verify its practical functioning in terms of accuracy and conservation properties. Finally, in Section 4, key findings are summarised and conclusions are drawn.

2. DG2 formulations on quadrilateral elements

This section explores DG2 numerical solutions for hyperbolic conservation laws over a 2D domain Ω. These can be written in the following conservative form:

$$\partial_t \mathbf{U} + \partial_x \mathbf{F}(\mathbf{U}) + \partial_y \mathbf{G}(\mathbf{U}) = \mathbf{S}(\mathbf{U}) \tag{1}$$

where $\mathbf{U}(x, y, t)$ is the vector of the state variables at the generic location (x, y) and time t, $\mathbf{F}(\mathbf{U})$ and $\mathbf{G}(\mathbf{U})$ are the spatial flux vectors relative to the two Cartesian directions, and $\mathbf{S}(\mathbf{U})$ is a vector including source terms. In (1), ∂_t, ∂_x and ∂_y represent partial derivatives with respect to t, x and y, respectively.

2.1. Standard form

The 2D domain Ω is discretised by means of $M \times N$ non-overlapping and uniform quadrilaterals Q_c ($c = 1, \ldots, M \times N$). By denoting (x_c, y_c) to be the centre of a quadrilateral Q_c and $\Delta x \times \Delta y$ its dimensions, Q_c can be expressed as $Q_c = [x_c - \Delta x/2, x_c + \Delta x/2] \times [y_c - \Delta y/2, y_c + \Delta y/2]$. A quadrilateral Q_c can be further mapped into the reference element $[-1, 1]^2 = [-1, 1] \times [-1, 1]$ by the transformation $(x, y) \epsilon Q_c \rightarrow (\xi, \eta) \epsilon [-1, 1]^2$ where $\xi(x) = 2(x - x_c)/\Delta x$ and $\eta(y) = 2(y - y_c)/\Delta y$; therefore $x(\xi) = x_c + \xi(\Delta x/2)$ and $y(\eta) = y_c + \eta(\Delta y/2)$ can be used to position Q_c onto $[-1, 1]^2$.

2.1.1. Finite element weak formulation

An approximate solution $\mathbf{U_h}$ of (1) is sought by multiplying both hand sides by a test function $v_h(x, y)$ that is compactly supported on Q_c and then integrating over Ω. This yields the following weak form:

$$\iint_{Q_c} \partial_t \mathbf{U_h}(x, y, t) v_h(x, y) \, dx dy + \iint_{Q_c} \partial_x \mathbf{F}(\mathbf{U_h}) v_h(x, y) \, dx dy + \iint_{Q_c} \partial_y \mathbf{G}(\mathbf{U_h}) v_h(x, y) \, dx dy =$$
$$\iint_{Q_c} \mathbf{S}(\mathbf{U_h}) v_h(x, y) \, dx dy \tag{2}$$

Integration by parts of the second and third terms at LHS of Eq. (2) gives:

$$\iint_{Q_c} \partial_x \mathbf{F}(\mathbf{U_h}) v_h(x, y) \, dx dy = \left[\int_{y_c - \Delta y/2}^{y_c + \Delta y/2} \mathbf{F}(\mathbf{U_h}) v_h(x, y) \, dy \right]_{x_c - \Delta x/2}^{x_c + \Delta x/2} - \iint_{Q_c} \mathbf{F}(\mathbf{U_h}) \partial_x v_h(x, y) \, dx dy \tag{3}$$

$$\iint_{Q_c} \partial_y \mathbf{G}(\mathbf{U_h}) v_h(x, y) \, dx dy = \left[\int_{x_c - \Delta x/2}^{x_c + \Delta x/2} \mathbf{G}(\mathbf{U_h}) v_h(x, y) \, dy \right]_{y_c - \Delta y/2}^{y_c + \Delta y/2} - \iint_{Q_c} \mathbf{G}(\mathbf{U_h}) \partial_y v_h(x, y) \, dx dy \tag{4}$$

Note that in Eqs. (3)–(4) the spatial derivatives are now removed from the flux terms. By plugging (3) and (4) into (2), and moving the spatial components to the RHS of the equation, the weak form can be expressed as:

$$\iint_{Q_c} \partial_t \mathbf{U_h}(x, y, t) v_h(x, y)\, dxdy = \mathbf{L_h} \tag{5}$$

$$\mathbf{L_h} = -\left[(\mathbf{I_h} + \mathbf{J_h}) - (\mathbf{M_h} + \mathbf{N_h} + \mathbf{S_h})\right] \tag{6}$$

In the spatial operator $\mathbf{L_h}$, $\mathbf{I_h}$ and $\mathbf{J_h}$ are local flux balance terms throughout the x- and y-direction, respectively:

$$\mathbf{I_h} = \left[\int_{y_c-\Delta y/2}^{y_c+\Delta y/2} \mathbf{F}(\mathbf{U_h}) v_h(x, y)\, dy\right]_{x_c-\Delta x/2}^{x_c+\Delta x/2} \tag{7}$$

$$\mathbf{J_h} = \left[\int_{x_c-\Delta x/2}^{x_c+\Delta x/2} \mathbf{G}(\mathbf{U_h}) v_h(x, y)\, dy\right]_{y_c-\Delta y/2}^{y_c+\Delta y/2} \tag{8}$$

and, $\mathbf{M_h}$, $\mathbf{N_h}$ and $\mathbf{S_h}$ are local volume integral terms for the fluxes and the source terms, that is:

$$\mathbf{M_h} = \iint_{Q_c} \mathbf{F}(\mathbf{U_h}) \partial_x v_h(x, y)\, dxdy \tag{9}$$

$$\mathbf{N_h} = \iint_{Q_c} \mathbf{G}(\mathbf{U_h}) \partial_y v_h(x, y)\, dxdy \tag{10}$$

$$\mathbf{S_h} = \iint_{Q_c} \mathbf{S}(\mathbf{U_h}) v_h(x, y)\, dxdy \tag{11}$$

2.1.2. Choice of 2D local basis functions

To construct a local planar DG2 solution on quadrilaterals, a suitable choice for the test function v_h is via the 2D tensor product of the Legendre basis truncated to first-order monomials. This yields an orthogonal basis over $[-1, 1]^2$ which can be expressed as:

$$\boldsymbol{\phi} = \{\varphi^0, \varphi^{1x}, \varphi^{1y}\} \text{ with } \varphi^0(\xi, \eta) = 1, \varphi^{1x}(\xi, \eta) = \xi, \quad \text{and} \quad \varphi^{1y}(\xi, \eta) = \eta \tag{12}$$

Over this basis, the stencil of a quadrilateral element Q_c is described in Fig. 1, and on which the following planar approximate solution $\mathbf{U_h}$ can be generated:

$$\mathbf{U_h}(x(\xi), y(\eta), t)|_{Q_c} = \mathbf{U_c^0}(t) + \xi \mathbf{U_c^{1x}}(t) + \eta \mathbf{U_c^{1y}}(t) \tag{13}$$

where $\mathbf{U_c^0}(t)$, $\mathbf{U_c^{1x}}(t)$ and $\mathbf{U_c^{1y}}(t)$ are the expansion coefficients that need to be initialised (Section 2.1.3), and updated by spatial evolution operators (Section 2.1.4) obtained by substituting the basis in (12) and the expansion in (13) into Eqs. (5) and (6).

2.1.3. Initialisation of the evolution coefficients

For a given initial value of the state variables $\mathbf{U}(x, y, 0) = \mathbf{U_0}(x, y)$, coefficients $\mathbf{U_c^0}(0)$, $\mathbf{U_c^{1x}}(0)$ and $\mathbf{U_c^{1y}}(0)$ over Q_c can be obtained by the following local projection on the planar basis (12):
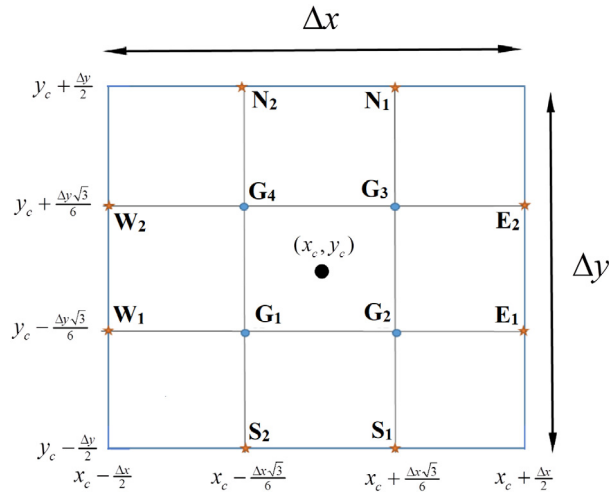
$$\mathbf{U_c^0}(0) = \frac{1}{\Delta x}\frac{1}{\Delta y} \iint_{Q_c} \mathbf{U_0}(x(\xi), y(\eta))dxdy = \frac{1}{4} \iint_{[-1,1]^2} \mathbf{U_0}(\xi, \eta)\, d\xi d\eta \tag{14}$$

$$\mathbf{U_c^{1x}}(0) = \frac{3}{\Delta x}\frac{1}{\Delta y} \iint_{Q_c} \mathbf{U_0}(x(\xi), y(\eta))\xi dxdy = \frac{3}{4} \iint_{[-1,1]^2} \xi \mathbf{U_0}(\xi, \eta)\, d\xi d\eta \tag{15}$$

$$\mathbf{U_c^{1y}}(0) = \frac{1}{\Delta x}\frac{3}{\Delta y} \iint_{Q_c} \mathbf{U_0}(x(\xi), y(\eta))\eta dxdy = \frac{3}{4} \iint_{[-1,1]^2} \eta \mathbf{U_0}(\xi, \eta)\, d\xi d\eta \tag{16}$$

The integrals in Eqs. (14)–(16) can be calculated using the following 2D Gaussian quadrature rule:

$$\iint_{[-1,1]^2} r(\xi, \eta)\, d\xi d\eta \approx r\left(\frac{1}{\sqrt{3}}, \frac{1}{\sqrt{3}}\right) + r\left(-\frac{1}{\sqrt{3}}, \frac{1}{\sqrt{3}}\right) + r\left(\frac{1}{\sqrt{3}}, -\frac{1}{\sqrt{3}}\right) + r\left(-\frac{1}{\sqrt{3}}, -\frac{1}{\sqrt{3}}\right) \tag{17}$$

Fig. 1. Stencil of a quadrilateral element Q_c for the standard DG2 form based on 2D tensor product of Legendre basis functions. G_i ($i = 1, 2, 3$ and 4) indicate local Gaussian points by which the volume integral terms in (9)–(11) are approximated via Eq. (17). E_i, W_i, N_i and S_i ($i = 1,2$) are Gaussian points located at the eastern, western, northern and southern faces, respectively, for aggregating normal (Riemann) fluxes contribution (see Eqs. (24)–(25)).

so that the following explicit formulae for initialising $\mathbf{U_h}(x, y, 0)\,|_{Q_c}$ (see Fig. 1) are derived:

$$\mathbf{U}_c^0(0) = \frac{1}{4}\left[\mathbf{U_0}(G_1) + \mathbf{U_0}(G_2) + \mathbf{U_0}(G_3) + \mathbf{U_0}(G_4)\right] \tag{18}$$

$$\mathbf{U}_c^{1x}(0) = \frac{\sqrt{3}}{4}\left[\mathbf{U_0}(G_3) - \mathbf{U_0}(G_4) + \mathbf{U_0}(G_2) - \mathbf{U_0}(G_1)\right] \tag{19}$$

$$\mathbf{U}_c^{1y}(0) = \frac{\sqrt{3}}{4}\left[\mathbf{U_0}(G_3) - \mathbf{U_0}(G_2) + \mathbf{U_0}(G_4) - \mathbf{U_0}(G_1)\right] \tag{20}$$

where G_i ($i = 1, \ldots, 4$) are 2D Gaussian points mapped from the reference element (Fig. 1), i.e.:

$$G_i = \left(x\left(\frac{\pm 1}{\sqrt{3}}\right), y\left(\frac{\pm 1}{\sqrt{3}}\right)\right) = \left(x_c \pm \frac{\sqrt{3}}{6}\Delta x, y_c \pm \frac{\sqrt{3}}{6}\Delta y\right) \tag{21}$$

2.1.4. Discrete spatial operators

By exploiting the orthogonality property of the Legendre basis and employing the planar expansion (13), the system can be rewritten in the following decoupled form:

$$\Delta x\,\Delta y \begin{pmatrix} \partial_t\mathbf{U}_c^0(t) & 0 & 0 \\ 0 & \partial_t\mathbf{U}_c^{1x}(t)/3 & 0 \\ 0 & 0 & \partial_t\mathbf{U}_c^{1y}(t)/3 \end{pmatrix} = \begin{pmatrix} \mathbf{L}_c^0 & 0 & 0 \\ 0 & \mathbf{L}_c^{1x} & 0 \\ 0 & 0 & \mathbf{L}_c^{1y} \end{pmatrix} \tag{22}$$

where $\mathbf{L}_c^0$, $\mathbf{L}_c^{1x}$ and $\mathbf{L}_c^{1y}$ denote local discrete spatial operators needed to update the coefficients $\mathbf{U}_c^0$, $\mathbf{U}_c^{1x}$ and $\mathbf{U}_c^{1y}$. Their expression can be obtained by considering Eq. (6) alongside Eqs. (12) and (13):

$$\mathbf{L}_c^K = -\left[(\mathbf{I}_c^K + \mathbf{J}_c^K) - (\mathbf{M}_c^K + \mathbf{N}_c^K + \mathbf{S}_c^K)\right] \quad (K = 0, 1x, 1y) \tag{23}$$

The physical fluxes involved in the discrete flux balance terms, $\mathbf{I}_c^K$ and $\mathbf{J}_c^K$, are replaced by numerical flux functions based on an approximate Riemann solver [10,11], i.e. $\tilde{\mathbf{F}}$ and $\tilde{\mathbf{G}}$, for resolving solution discontinuities at the faces between adjacent elements. In this work, the Roe Riemann solver [77] is used to define $\tilde{\mathbf{F}}$ and $\tilde{\mathbf{G}}$. By further using Eq. (17) to eliminate the integral terms in Eqs. (7)–(8), the following discrete forms for $\mathbf{I}_c^K$ and $\mathbf{J}_c^K$, are obtained (see also Fig. 1):

$$\mathbf{I}_c^K = \Delta y\left\{\frac{1}{2}\left[\tilde{\mathbf{F}}\left(\mathbf{U_h}\left(E_1^-, t\right), \mathbf{U_h}\left(E_1^+, t\right)\right)\varphi^K\left(1, \tfrac{-1}{\sqrt{3}}\right) + \tilde{\mathbf{F}}\left(\mathbf{U_h}\left(E_2^-, t\right), \mathbf{U_h}\left(E_2^+, t\right)\right)\varphi^K\left(1, \tfrac{1}{\sqrt{3}}\right)\right]\right\}$$

$$-\frac{1}{2}\left[\tilde{\mathbf{F}}\left(\mathbf{U_h}\left(W_1^-,t\right),\mathbf{U_h}\left(W_1^+,t\right)\right)\varphi^K(-1,\tfrac{-1}{\sqrt{3}})+\tilde{\mathbf{F}}\left(\mathbf{U_h}\left(W_2^-,t\right),\mathbf{U_h}\left(W_2^+,t\right)\right)\varphi^K(-1,\tfrac{1}{\sqrt{3}})\right]\right\} \tag{24}$$

$$\mathbf{J}_c^K = \Delta x\left\{\frac{1}{2}\left[\tilde{\mathbf{G}}\left(\mathbf{U_h}\left(N_1^-,t\right),\mathbf{U_h}\left(N_1^+,t\right)\right)\varphi^K(\tfrac{-1}{\sqrt{3}},1)+\tilde{\mathbf{G}}\left(\mathbf{U_h}\left(N_2^-,t\right),\mathbf{U_h}\left(N_2^+,t\right)\right)\varphi^K(\tfrac{1}{\sqrt{3}},1)\right]\right.$$

$$\left.-\frac{1}{2}\left[\tilde{\mathbf{G}}\left(\mathbf{U_h}\left(S_1^-,t\right),\mathbf{U_h}\left(S_1^+,t\right)\right)\varphi^K(\tfrac{-1}{\sqrt{3}},-1)+\tilde{\mathbf{G}}\left(\mathbf{U_h}\left(S_2^-,t\right),\mathbf{U_h}\left(S_2^+,t\right)\right)\varphi^K(\tfrac{1}{\sqrt{3}},-1)\right]\right\} \tag{25}$$

where $K = 0, 1x, 1y$ with φ^K being the associated component of the basis functions in Eq. (12). In Eq. (24), as can also been seen in Fig. 1, $E_{1,2} = (x\,(1)\,,y(\pm 1/\sqrt{3})) = (x_c + \frac{\Delta x}{2}, y_c \pm \frac{\sqrt{3}}{6}\Delta y)$ and $W_{1,2} = (x\,(-1)\,,y(\pm 1/\sqrt{3})) = (x_c - \frac{\Delta x}{2}, y_c \pm \frac{\sqrt{3}}{6}\Delta y)$ are Gaussian integration points located at the eastern and western faces, respectively, where the x-directional and Riemann flux $\tilde{\mathbf{F}}$ is evaluated for averaging across the face. In Eq. (25), $N_{1,2} = (x(\pm 1/\sqrt{3}),\,y\,(1)) = (x_c \pm \frac{\sqrt{3}}{6}\Delta x, y_c + \frac{\Delta y}{2})$ and $S_{1,2} = (x(\pm 1/\sqrt{3}),\,y\,(-1)) = (x_c \pm \frac{\sqrt{3}}{6}\Delta x, y_c - \frac{\Delta y}{2})$ are the Gaussian integration points located at the northern and southern faces, respectively, where the y-directional Riemann flux $\tilde{\mathbf{G}}$ is evaluated for averaging across the face.

The terms involving volume integrals of the fluxes $\mathbf{M}_c^K$ and $\mathbf{N}_c^K$ can be obtained by replacing Eqs. (12)–(13) into Eqs. (9)–(10) and apply (17), yielding the following expressions (see also Fig. 1):

$$\mathbf{M}_c^K = \begin{cases} 0 & (K = 0, 1y) \\ \frac{\Delta y}{2}\left[\mathbf{F}\left(\mathbf{U_h}\left(G_1,t\right)\right)+\mathbf{F}\left(\mathbf{U_h}\left(G_2,t\right)\right)+\mathbf{F}\left(\mathbf{U_h}\left(G_3,t\right)\right)+\mathbf{F}\left(\mathbf{U_h}\left(G_4,t\right)\right)\right] & (K = 1x) \end{cases} \tag{26}$$

$$\mathbf{N}_c^K = \begin{cases} 0 & (K = 0, 1x) \\ \frac{\Delta x}{2}\left[\mathbf{G}\left(\mathbf{U_h}\left(G_1,t\right)\right)+\mathbf{G}\left(\mathbf{U_h}\left(G_2,t\right)\right)+\mathbf{G}\left(\mathbf{U_h}\left(G_3,t\right)\right)+\mathbf{G}\left(\mathbf{U_h}\left(G_4,t\right)\right)\right] & (K = 1y) \end{cases} \tag{27}$$

The volume integrals of the source terms $\mathbf{S}_c^K$, in Eq. (11) can be approximated via direct application of the 2D quadrature rule in Eq. (17), as done in Section 2.1.3, to give (see also Fig. 1):

$$\mathbf{S}_c^K = \begin{cases} \dfrac{\Delta x\,\Delta y}{4}\left[\mathbf{S}\left(\mathbf{U_h}\left(G_1,t\right)\right)+\mathbf{S}\left(\mathbf{U_h}\left(G_2,t\right)\right)+\mathbf{S}\left(\mathbf{U_h}\left(G_3,t\right)\right)+\mathbf{S}\left(\mathbf{U_h}\left(G_4,t\right)\right)\right] & (K = 0) \\ \dfrac{\Delta x\,\Delta y\sqrt{3}}{12}\left[\mathbf{S}\left(\mathbf{U_h}\left(G_2,t\right)\right)-\mathbf{S}\left(\mathbf{U_h}\left(G_1,t\right)\right)+\mathbf{S}\left(\mathbf{U_h}\left(G_3,t\right)\right)-\mathbf{S}\left(\mathbf{U_h}\left(G_4,t\right)\right)\right] & (K = 1x) \\ \dfrac{\Delta x\,\Delta y\sqrt{3}}{12}\left[\mathbf{S}\left(\mathbf{U_h}\left(G_3,t\right)\right)-\mathbf{S}\left(\mathbf{U_h}\left(G_2,t\right)\right)+\mathbf{S}\left(\mathbf{U_h}\left(G_4,t\right)\right)-\mathbf{S}\left(\mathbf{U_h}\left(G_1,t\right)\right)\right] & (K = 1y) \end{cases} \tag{28}$$

2.1.5. Some remarks

The spatial DG2 discretisation outlined through Eqs. (23)–(28) is applied within a two-stage Runge–Kutta (RK) time stepping to form the so-called RKDG2 method. Each RK stage should be preceded by the application of a slope limiter to ensure that local DG2 slope coefficients, i.e. $\mathbf{U}_c^{1x}$ and $\mathbf{U}_c^{1y}$, have limited variations relating to slopes differentiated from the means at Q_c and its adjacent neighbours. However, it is useful to make some notes about a number of key points relevant to this DG2 structure.

Cross-dimensional slope dependency. The slope evolution operators $\mathbf{L}_c^{1x}$ and $\mathbf{L}_c^{1y}$, although aimed to update the x- and y-directional slope coefficients $\mathbf{U}_c^{1x}$ and $\mathbf{U}_c^{1y}$ still depends on both slope coefficients, mainly due to the location of the evaluation points in the stencil (Fig. 1). In effect, at any of the relevant evaluation points – namely E_i, W_i, N_i and S_i ($i = 1, 2$) and G_i ($i = 1, 2, 3, 4$) in Fig. 1 – the local planar solution $\mathbf{U}_h|_{Q_c}$ reads:

$$\mathbf{U}_h\left(E_i,t\right) = \mathbf{U}_c^0\left(t\right)+\mathbf{U}_c^{1x}\left(t\right)\pm\frac{\mathbf{U}_c^{1y}\left(t\right)}{\sqrt{3}} \quad (i = 1, 2) \tag{29a}$$

$$\mathbf{U}_h\left(W_i,t\right) = \mathbf{U}_c^0\left(t\right)-\mathbf{U}_c^{1x}\left(t\right)\pm\frac{\mathbf{U}_c^{1y}\left(t\right)}{\sqrt{3}} \quad (i = 1, 2) \tag{29b}$$

$$\mathbf{U}_h\left(N_i,t\right) = \mathbf{U}_c^0\left(t\right)\pm\frac{\mathbf{U}_c^{1x}\left(t\right)}{\sqrt{3}}+\mathbf{U}_c^{1y}\left(t\right) \quad (i = 1, 2) \tag{30a}$$
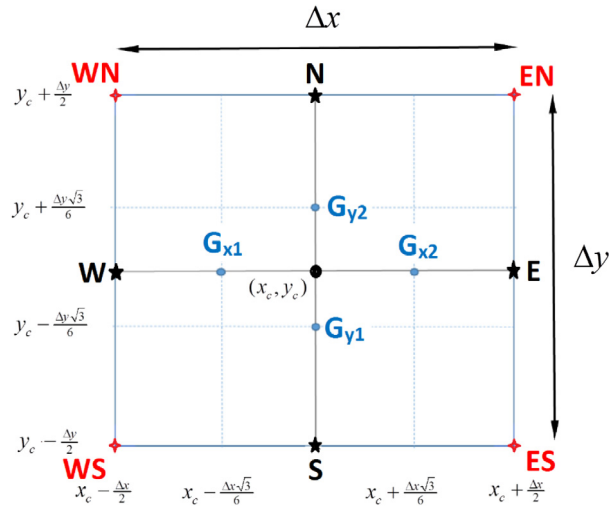
Fig. 2. Stencil of a quadrilateral element Q_c for the proposed slope-decoupled DG2 form. Here, two different sets of 1D Gaussian points $\{G_{xi}\}_{i=1,2}$ and $\{G_{yi}\}_{i=1,2}$ are involved in an entirely decoupled manner along the *x*-directional and *y*-directional centrelines, respectively. Also, one evaluation for the normal (Riemann) flux at any of the four faces is sought in this setting, i.e. at the centres E and W of the eastern and western faces in alignment with $[G_{x1}, G_{x2}]$ and N and S of the northern and southern faces in alignment with $[G_{y1}, G_{y2}]$. EN, ES, WS and WN denote the corner points of Q_c named, respectively, according to the two faces they span (e.g., WS stands for the corner point at which the western and southern faces intersect).

$$\mathbf{U}_h(\mathbf{S}_i, t) = \mathbf{U}_c^0(t) \pm \frac{\mathbf{U}_c^{1x}(t)}{\sqrt{3}} - \mathbf{U}_c^{1y}(t) \quad (i = 1, 2) \tag{30b}$$

$$\mathbf{U}_h(\mathbf{G}_i, t) = \mathbf{U}_c^0(t) \pm \frac{\mathbf{U}_c^{1x}(t)}{\sqrt{3}} \pm \frac{\mathbf{U}_c^{1y}(t)}{\sqrt{3}} \quad (i = 1, \ldots, 4) \tag{31}$$

for which, as clear in Eqs. (29)–(31), none of the slope coefficients vanishes in any of the evaluations.

Impact of the slope limiter. The slope limiter in DG methods comes in as a finite volume tool aimed to stabilise the solution around sharp discontinuities (i.e. avoid the development of the Gibbs phenomenon). Nonetheless, it is generally demonstrated that slope limiters may have adverse effects such as distorting the solution around smooth areas [43,53–61]. To reduce such an impact on DG predictions, the slope limiting process may be localised based on the so-called troubled-cell indicator [47], such as the shock detector in [53] that will be used in this work. However, given the cross-dimensional slope dependency issue raised above, any potential impact due to slope limiting would be omnipresent across all the evaluations.

Operational costs. Over each RK stage, the DG2 discretisation requires solving for 8 different Riemann problems to calculate the flux balance terms, 8 Gaussian point evaluations to calculate the flux volume integrals, and 16 Gaussian point evaluations to calculate approximations of the volume integrals of the source terms. Hence, at least 32 spatial operations are needed to enable progressing the state of the solution over one element by half a time step, which is computationally expensive.

2.2. Slope-decoupled form

In this section, a simplified DG2 formulation is presented using the same choice for the local basis functions as in Section 2.1, but based upon a different local stencil, which is described in Fig. 2. As shown in the figure, now two different sets of Gaussian points $\{G_{xi}\}_{i=1,2}$ and $\{G_{yi}\}_{i=1,2}$ are involved in an entirely 1D decoupled manner along the *x*-directional and *y*-directional centrelines, respectively, via a standard 1D two-point Gauss–Legendre rule. In this setting, the set $\{G_{xi}\}_{i=1,2}$ is applied to approximate all the integral terms in the operator $\mathbf{L}_c^{1x}$, considering no variation

occur along the y-direction. Similarity, the set $\left\{G_{yi}\right\}_{i=1,2}$ is used to approximate all the integral terms in the operator $\mathbf{L}_c^{\mathbf{1y}}$ considering no variation occur along the x-direction. Also, only one evaluation for the flux at any of the four faces is required, namely at the centres E and W of the eastern and western faces, and N and S of the northern and southern faces, located on the centreline $[G_{x1}, G_{x2}]$, respectively $[G_{y1}, G_{y2}]$. The main purpose from adopting this stencil is to decouple the slope dependencies in Cartesian directions. That is, it can be easily shown that over the stencil depicted in Fig. 2, as opposed to Eqs. (29)–(31), any local solution evaluation at the relevant points only involves one slope coefficient, namely:

$$\mathbf{U}_h (\mathrm{E}, t) = \mathbf{U}_c^{\mathbf{0}} (t) + \mathbf{U}_c^{\mathbf{1x}} (t) \tag{32a}$$

$$\mathbf{U}_h (\mathrm{W}, t) = \mathbf{U}_c^{\mathbf{0}} (t) - \mathbf{U}_c^{\mathbf{1x}} (t) \tag{32b}$$

$$\mathbf{U}_h (\mathrm{N}, t) = \mathbf{U}_c^{\mathbf{0}} (t) + \mathbf{U}_c^{\mathbf{1y}} (t) \tag{33a}$$

$$\mathbf{U}_h (\mathrm{S}, t) = \mathbf{U}_c^{\mathbf{0}} (t) - \mathbf{U}_c^{\mathbf{1y}} (t) \tag{33b}$$

$$\mathbf{U}_\mathrm{h} (G_{xi}, t) = \mathbf{U}_c^{\mathbf{0}} (t) \pm \frac{\mathbf{U}_c^{\mathbf{1x}} (t)}{\sqrt{3}} \quad (i = 1, 2) \tag{34a}$$

$$\mathbf{U}_h \left(G_{yi}, t\right) = \mathbf{U}_c^{\mathbf{0}} (t) \pm \frac{\mathbf{U}_c^{\mathbf{1y}} (t)}{\sqrt{3}} \quad (i = 1, 2) \tag{34b}$$

Eqs. (32)–(34) result in the sole involvement of the x-directional (y-directional) slope coefficient in the evaluation of the Riemann problem and integral terms involving the x-directional flux $\mathbf{F}$ (y-directional $\mathbf{G}$) within the $\mathbf{L}_c^0$, $\mathbf{L}_c^{1x}$ and $\mathbf{L}_c^{1y}$ local spatial operators. Considering also that the x-directional and y-directional variations of the local planar solution are zero along the y-direction and x-direction, the terms $\mathbf{I}_c^K$, $\mathbf{J}_c^K$, $\mathbf{M}_c^K$, $\mathbf{N}_c^K$ and $\mathbf{S}_c^K$ become:

$$\mathbf{I}_c^K = \Delta y \left\{ \tilde{\mathbf{F}} \left(\mathbf{U_h} \left(\mathrm{E}^-, t\right), \mathbf{U_h} \left(\mathrm{E}^+, t\right)\right) \varphi^K (1, 0) - \tilde{\mathbf{F}} \left(\mathbf{U_h} \left(\mathrm{W}^-, t\right), \mathbf{U_h} \left(\mathrm{W}^+, t\right)\right) \varphi^K (-1, 0) \right\} \tag{35}$$

$$\mathbf{J}_c^K = \Delta x \left\{ \tilde{\mathbf{G}} \left(\mathbf{U_h} \left(N^-, t\right), \mathbf{U_h} \left(N^+, t\right)\right) \varphi^K (0, 1) - \tilde{\mathbf{G}} \left(\mathbf{U_h} \left(S^-, t\right), \mathbf{U_h} \left(S^+, t\right)\right) \varphi^K (0, -1) \right\} \tag{36}$$

$$\mathbf{M}_c^K = \begin{cases} 0 & (K = 0, 1y) \\ \Delta y \left[\mathbf{F} \left(\mathbf{U_h} (G_{x2}, t)\right) + \mathbf{F} \left(\mathbf{U_h} (G_{x1}, t)\right)\right] & (K = 1x) \end{cases} \tag{37}$$

$$\mathbf{N}_c^K = \begin{cases} 0 & (K = 0, 1x) \\ \Delta x \left[\mathbf{G} \left(\mathbf{U_h} \left(G_{y2}, t\right)\right) + \mathbf{G} \left(\mathbf{U_h} \left(G_{y1}, t\right)\right)\right] & (K = 1y) \end{cases} \tag{38}$$

$$\mathbf{S}_c^K = \begin{cases} \Delta x \Delta y \left[\mathbf{S} \left(\mathbf{U_h} \left((x_c, y_c), t\right)\right)\right] & (K = 0) \\ \dfrac{\Delta x \Delta y \sqrt{3}}{6} \left[\mathbf{S} \left(\mathbf{U_h} (G_{x2}, t)\right) - \mathbf{S} \left(\mathbf{U_h} (G_{x1}, t)\right)\right] & (K = 1x) \\ \dfrac{\Delta x \Delta y \sqrt{3}}{6} \left[\mathbf{S} \left(\mathbf{U_h} \left(G_{y2}, t\right)\right) - \mathbf{S} \left(\mathbf{U_h} \left(G_{y1}, t\right)\right)\right] & (K = 1y) \end{cases} \tag{39}$$

In Eq. (39), $\mathbf{S}_c^0$ represents an approximation of source terms achieved by a mid-point rule. Considering further the properties of the Legendre basis, i.e. $\varphi^0 (\xi, \eta) = 1$, $\varphi^{1x} (\pm 1, 0) = \varphi^{1y} (0, \pm 1) = \pm 1$, and the scaling factors in Eq. (22), the following evolution operators can be obtained for updating the average and slope coefficients over Q_c over a RK time stage:

$$\mathbf{L}_c^0 = -\frac{1}{\Delta x} \left(\tilde{\mathbf{F}}_\mathrm{E} - \tilde{\mathbf{F}}_\mathrm{W}\right) - \frac{1}{\Delta y} \left(\tilde{\mathbf{F}}_\mathrm{N} - \tilde{\mathbf{F}}_\mathrm{S}\right) + \mathbf{S}(\mathbf{U_h} \left((x_\mathrm{c}, y_\mathrm{c}), t\right)) \tag{40}$$

$$\mathbf{L}_c^{1x} = -\frac{3}{\Delta x} \left\{ \left(\tilde{\mathbf{F}}_\mathrm{E} + \tilde{\mathbf{F}}_\mathrm{W}\right) - \left(\mathbf{F} \left(\mathbf{U_h} (G_{x2}, t)\right) + \mathbf{F} \left(\mathbf{U_h} (G_{x1}, t)\right)\right) \right.$$
$$\left. - \frac{\Delta x \sqrt{3}}{6} \left[\mathbf{S} \left(\mathbf{U_h} (G_{x2}, t)\right) - \mathbf{S} \left(\mathbf{U_h} (G_{x1}, t)\right)\right] \right\} \tag{41}$$

$$
\mathbf{L}_c^{1y} = -\frac{3}{\Delta y} \left\{ \left(\tilde{\mathbf{F}}_N + \tilde{\mathbf{F}}_S \right) - \left(\mathbf{G}\left(\mathbf{U_h}\left(G_{y2}, t \right) \right) + \mathbf{G}\left(\mathbf{U_h}\left(G_{y1}, t \right) \right) \right) \right.
$$
$$
\left. - \frac{\Delta y \sqrt{3}}{6} \left[\mathbf{S}\left(\mathbf{U_h}\left(G_{y2}, t \right) \right) - \mathbf{S}\left(\mathbf{U_h}\left(G_{y1}, t \right) \right) \right] \right\}
\tag{42}
$$

where $\tilde{\mathbf{F}}_E = \tilde{\mathbf{F}}\left(\mathbf{U_h}\left(E^-, t \right), \mathbf{U_h}\left(E^+, t \right) \right)$, $\tilde{\mathbf{F}}_W = \tilde{\mathbf{F}}\left(\mathbf{U_h}\left(W^-, t \right), \mathbf{U_h}\left(W^+, t \right) \right)$, $\tilde{\mathbf{F}}_N = \tilde{\mathbf{F}}\left(\mathbf{U_h}\left(N^-, t \right), \mathbf{U_h}\left(N^+, t \right) \right)$ and $\tilde{\mathbf{F}}_S = \tilde{\mathbf{F}}\left(\mathbf{U_h}\left(S^-, t \right), \mathbf{U_h}\left(S^+, t \right) \right)$ represent the Riemann flux evaluations across the eastern, western, northern and southern faces of the element Q_c, considering the limited slope coefficients in (32)–(34) with the same localised slope limiter as in the standard form (Section 2.1). When compared to the standard DG2 form, the simplified scheme (40)–(42) reduces the total number of operations from 32 to 12 (4 Riemann problem solutions and 8 Gaussian point evaluations), leading to a drastic reduction in operational cost. The simplified DG2 is therefore predicted to offer speed up in runtime relative to the standard DG2 form by a factor of 2.6 (see also Section 3.1.1). It has also the advantage of being well-balanced for all average and slope coefficients as shown in Section 2.2.1.

2.2.1. Shallow water equations with topography

The conventional form of the SWE [76] can be expressed by Eq. (1) by assuming:

$$
\mathbf{U} = \begin{bmatrix} h \\ q_x \\ q_y \end{bmatrix}, \mathbf{F} = \begin{bmatrix} q_x \\ \dfrac{q_x^2}{h} + \dfrac{g}{2}h^2 \\ \dfrac{q_x q_y}{h} \end{bmatrix}, \mathbf{G} = \begin{bmatrix} q_y \\ \dfrac{q_x q_y}{h} \\ \dfrac{q_y^2}{h} + \dfrac{g}{2}h^2 \end{bmatrix} \quad \text{and} \quad \mathbf{S} = \begin{bmatrix} 0 \\ -gh\partial_x z \\ -gh\partial_y z \end{bmatrix}
\tag{43}
$$

where $h(x, y, t)$ represents the water depth (L), $q_x = hu$ and $q_y = hv$ are volumetric discharges per unit width (L^2/T) expressed in terms of the velocities $u(x, y, t)$ and $v(x, y, t)$ along the Cartesian directions (L/T), g represents the acceleration due to gravity (L/T²), and $\partial_x z$ and $\partial_y z$ are the partial derivatives of a topography function $z(x, y)$.

When $z(x, y) \neq 0$, the system of Eqs. (1) and (43) may be referred to as non-homogeneous hyperbolic conservation laws [2]. A known challenge [2] is to find *a straightforward discretisation of the source terms* that balances the flux gradients when the flow admits steady state solutions, that is produces a well-balanced DG2 scheme. In principle, such a scheme should preserve the *still water* stationary solution over an uneven topography [2], for which the initial conditions are:

$$
h + z = constant \quad \text{and} \quad \left(q_x, q_y \right) = (0, 0)
\tag{44}
$$

In the context of practical hydraulic simulations, the design of a well-balanced DG2 scheme with the condition (44) faces numerous challenges, including: (a) the DG2 scheme should verify the discrete balance between the gradients of the fluxes and the topography for any wetting and drying scenarios in the computational domains such as when a planar solution intersects with the topography; (b) the DG2 scheme should remain stable for a flow over a steep terrain, e.g. a building-like block, where the topography function is not differentiable; (c) all DG2 operators (Eqs. (40)–(42)) should be well-balanced with respect to the average coefficient, $\mathbf{U}_c^0$, and the slope coefficients, $\mathbf{U}_c^{1x}$ and $\mathbf{U}_c^{1y}$, as well. In Sections 2.2.2 and 2.2.3 we demonstrate that the slope-decoupled DG2 operators offer a *simple approach* to effectively address these challenges.

2.2.2. Well-balancedness properties in a 1D case

As a background study, the system of Eqs. (1) with the variables (43) is first considered in the 1D case:

$$
\partial_t \mathbf{U} + \partial_x \mathbf{F}(\mathbf{U}) = \mathbf{S}(\mathbf{U})
\tag{45}
$$

$$
\mathbf{U} = \begin{bmatrix} h \\ q_x \end{bmatrix}, \mathbf{F} = \begin{bmatrix} q_x \\ \dfrac{q_x^2}{h} + \dfrac{g}{2}h^2 \end{bmatrix}, \quad \text{and} \quad \mathbf{S} = \begin{bmatrix} 0 \\ -gh\partial_x z \end{bmatrix}
\tag{46}
$$

In such case, the simplified DG2 operators reduce to:

$$
\mathbf{L}_c^0 = -\frac{1}{\Delta x}\left(\tilde{\mathbf{F}}_E - \tilde{\mathbf{F}}_W \right) + \mathbf{S}(\mathbf{U_h}(x_c, t))
\tag{47}
$$

$$\mathbf{L}_c^{1x} = -\frac{3}{\Delta x} \left\{ \left(\tilde{\mathbf{F}}_E + \tilde{\mathbf{F}}_W \right) - \left(\mathbf{F} \left(\mathbf{U_h} \left(G_{x2}, t \right) \right) + \mathbf{F} \left(\mathbf{U_h} \left(G_{x1}, t \right) \right) \right) \right.$$

$$\left. - \frac{\Delta x \sqrt{3}}{6} \left[\mathbf{S} \left(\mathbf{U_h} \left(G_{x2}, t \right) \right) - \mathbf{S} \left(\mathbf{U_h} \left(G_{x1}, t \right) \right) \right] \right\} \tag{48}$$

The initialisation of the local solution coefficients, given the initial condition $\mathbf{U}_0(x)$, can be obtained as in Section 2.1.3, but with further manipulation so as to involve only interface evaluations (details can be found in [78]):

$$\mathbf{U}_c^0(0) = \frac{1}{2} \left[\mathbf{U_0}(E) + \mathbf{U_0}(W) \right] \tag{49}$$

$$\mathbf{U}_c^{1x}(0) = \frac{1}{2} \left[\mathbf{U_0}(E) - \mathbf{U_0}(W) \right] \tag{50}$$

This form of modal initialisation by nodal evaluations is important for achieving a local linear projection of the topography function onto the DG2 space, denoted by $z_h(x)|_{Q_c}$, that is *globally continuous* over the domain, i.e.:

$$z_c^0 = \frac{1}{2} \left[z(E) + z(W) \right] \tag{51}$$

$$z_c^{1x} = \frac{1}{2} \left[z(E) - z(W) \right] \tag{52}$$

With this discretisation of the topography, the continuity property is easily verified, in particular across the interface points E and W. For example, at the eastern interface, E, which is shared by elements Q_c and Q_{c+1}, Eqs. (51) and (52) yield:

$$z_h \left(E^- \right)|_{Q_c} = z_c^0 + z_c^{1x} = z(E) = z_{c+1}^0 - z_{c+1}^{1x} = z_h \left(E^+ \right)|_{Q_{c+1}} \tag{53}$$

It is also easy to treat the bed slope source term in $\mathbf{S}$, via the slope coefficient in (52):

$$\partial_x z(x) \approx \partial_x z_h(x)|_{Q_c} = \frac{2}{\Delta x} z_c^{1x} \tag{54}$$

By initialising the slope coefficient of the topography as in Eqs. (51) and (52), the DG2 operators (47)–(48) become naturally well-balanced for cases involving a fully wet domain [78]. Nonetheless, such property can also be enforced for more general cases with wetting and drying by, (locally and temporarily) reapplying the modal projection Eqs. (49)–(52). By doing so, actions taken to ensure depth-positivity preserving reconstructions at the nodes are transferred into the modes while keeping the DG2 operators well-balanced.

In this work, the finite volume depth-positivity preserving reconstructions in [71] are applied at the nodes, however with the following simplifications:

- the conventional from of the SWE (45)–(46) are considered instead of the pre-balanced form;
- there is no intermediate involvement of the free-surface elevation variable;
- topography continuity (at the nodes), based on Eqs. (51)–(52), is ensured from the onset.

By denoting $\mathbf{U}_E^\pm = \mathbf{U}_h \left(E^\pm \right) = \left[h_E^\pm, (q_x)_E^\pm \right]^T$, $z_E = z_h(E^\pm)$, $\mathbf{U}_W^\pm = \mathbf{U}_h \left(W^\pm \right) = \left[h_W^\pm, (q_x)_W^\pm \right]^T$ and $z_W = z_h(W^\pm)$ as the nodal limits of the local linear solution at the interface E and W, respectively, and reconsidering the depth-positivity preserving reconstructions (see [71]), well-balanced positivity preserving versions can be obtained at the nodes and are denoted with the superscript "$*$":

$$h_W^{\pm,*} = max(0, h_W^\pm) \text{ and } (q_x)_W^{\pm,*} = h_W^{\pm,*} u_W^\pm \tag{55}$$

$$h_E^{\pm,*} = max(0, h_E^\pm) \text{ and } (q_x)_E^{\pm,*} = h_E^{\pm,*} u_E^\pm \tag{56}$$

where $u_W^+ = (q_x)_W^+ / h_W^+$ and $u_E^- = (q_x)_E^- / h_E^-$ when $h_h|_{Q_c} > tolh_{dry}$ or equal to zero otherwise. The parameter $tolh_{dry}$ is a threshold value for dry cells detection, which is here set equal to 10^{-4}. Further to Eqs. (55) and (56), the following (numerical) conditions for the nodal topography evaluations are necessary to also ensure stability at nodes where the flow depth is potentially negative:

$$z_W^* = z_W - max \left(0, -h_W^+ \right) \text{ and } z_E^* = z_E - max \left(0, -h_E^- \right) \tag{57}$$

It is worth noting that Eqs. (55)–(57) only act on the nodal evaluations (when wetting and drying is involved) for the states of the flow and/or topography variables, and also ensures continuity for the topography at the nodes. These potential changes in the nodal evaluations must then be used to consistently re-define *positivity-preserving modes*, which can be done by reapplying Eqs. (49)–(52) to re-initialise the modes as a subsequent step to Eqs. (55)–(57). This leads to revised modes for use in the DG2 operators (47) and (48), which are denoted with the "$^-$" symbol:

$$\overline{\mathbf{U}}_c^0 (t) = \frac{1}{2} \left[\mathbf{U}_E^{-,*} + \mathbf{U}_W^{+,*} \right] \tag{58}$$

$$\overline{\mathbf{U}}_c^{1x} (t) = \frac{1}{2} \left[\mathbf{U}_E^{-,*} - \mathbf{U}_W^{+,*} \right] \tag{59}$$

$$\overline{z}_c^{1x} = \frac{1}{2} \left[z_E^* - z_W^* \right] \tag{60}$$

We set now to demonstrate the well-balancedness property of the 1D case under consideration.

Theorem 1. *The proposed Eqs. (58)–(60) for the modes and Eqs. (55)–(57) for the nodes yield well-balanced DG2 spatial operators.*

Proof. Under the conditions established by Eqs. (44), $h + z = constant$ is particularly true at the local discrete level (i.e. for all elements Q_c given the continuity of z_h as per Eq. (53)), that is:

$$(h + z)_h = h_h + z_h = constant \tag{61}$$

After application of Eqs. (55)–(57) followed by Eqs. (58)–(60), the discrete still water in Eq. (61) can be expressed as:

$$\overline{h}_c^{1x} + \overline{z}_c^{1x} = 0 \tag{62}$$

$$\overline{h}_c^0 = \frac{h_E^{-,*} + h_W^{+,*}}{2} \quad \text{and} \quad \overline{h}_c^{1x} = \frac{h_E^{-,*} - h_W^{+,*}}{2} \tag{63}$$

$$\overline{z}_c^{1x} = \frac{z_E^* - z_W^*}{2} \tag{64}$$

Now, the local (i.e. over Q_c) approximate solution $\mathbf{U_h}$ is mainly the water depth variable h_h expressed by means of the positivity-preserving coefficients (63) alongside the bed slope coefficient (64). Terms from the flux and source vectors remain due to the hydrostatic balance equation remaining within the momentum equation (mass equation vanishes with the flow conditions in Eqs. (44)); they express as $f(h_h) = \frac{g}{2} h_h^2$ and $s(h_h) = -g h_h \partial_x z_h |_{Q_c}$ considering the coefficients in Eqs. (62)–(64) and (53).

Under conditions (62)–(64), with $\tilde{f}(h_E^{-,*}) = \frac{g}{2}(h_E^{-,*})^2$ and $\tilde{f}(h_W^{+,*}) = \frac{g}{2}(h_W^{+,*})^2$, the difference and sum of the Riemann flux evaluations can be manipulated to:

$$\tilde{f}(h_E^{-,*}) - \tilde{f}(h_W^{+,*}) = \frac{g}{2} \left[\left(2\overline{h}_c^0\right) \left(2\overline{h}_c^{1x}\right) \right] \tag{65}$$

$$\tilde{f}(h_E^{-,*}) + \tilde{f}(h_W^{+,*}) = \frac{g}{2} \left[2\left(\overline{h}_c^0\right)^2 + 2\left(\overline{h}_c^{1x}\right)^2 \right] \tag{66}$$
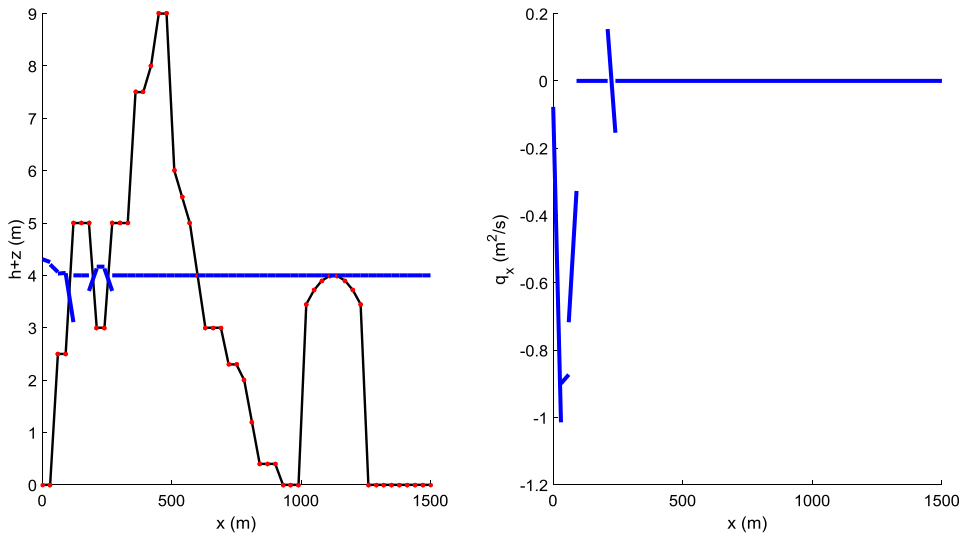
The local volume integral of the flux term (involved in the slope evolution operator (48)) becomes:

$$f(h_h(G_{x2})) + f(h_h(G_{x1})) = f\left(\overline{h}_c^0 + \frac{\overline{h}_c^{1x}}{\sqrt{3}}\right) + f\left(\overline{h}_c^0 - \frac{\overline{h}_c^{1x}}{\sqrt{3}}\right) = \frac{g}{2} \left[2\left(\overline{h}_c^0\right)^2 + \frac{2}{3}\left(\overline{h}_c^{1x}\right)^2 \right] \tag{67}$$

The source term evaluations (involved in both evolution operators (47) and (48)) becomes:

$$s(h_h(x_c)) = s\left(\overline{h}_c^0\right) = -g\overline{h}_c^0 \left(\frac{2\overline{z}_c^{1x}}{\Delta x}\right) \tag{68}$$

$$s(h_h(G_{x2})) - s(h_h(G_{x1})) = s\left(\overline{h}_c^0 + \frac{\overline{h}_c^{1x}}{\sqrt{3}}\right) - s\left(\overline{h}_c^0 - \frac{\overline{h}_c^{1x}}{\sqrt{3}}\right) = -g\left(\frac{2\overline{z}_c^{1x}}{\Delta x}\right) \left(\frac{\overline{h}_c^{1x}}{\sqrt{3}}\right) \tag{69}$$

Fig. 3. Simulation (using 50 cells and up to 20 s) of a still water state for assessing the well-balancedness of operators (47)–(48) without considering condition (57); "blue lines" = local linear DG2 flow solutions, "black lines" = local DG2 linear topography projections, "red markers" = nodal evaluations of the topography at interfaces. (For interpretation of the references to colour in this figure legend, the reader is referred to the web version of this article.)

Now the replacement of Eqs. (65)–(69) in operators (47)–(48) (for the remaining momentum terms), clearly produces discrete operators that become zero given the slope coefficients relationship in Eq. (62), $(-\overline{z}_c^{1x} = \overline{h}_c^{1x})$:

$$L_c^0 = -\frac{2g}{\Delta x}\left[\overline{h}_c^0\left(\overline{h}_c^{1x} + \overline{z}_c^{1x}\right)\right] \tag{70}$$

$$L_c^{1x} = -\frac{3g}{\Delta x}\left\{\frac{2}{3}\left(\overline{h}_c^{1x}\right)^2 - \frac{2}{3}\left[\left(-\overline{z}_c^{1x}\right)\left(\overline{h}_c^{1x}\right)\right]\right\} \tag{71}$$

Remark 1. In a fully wet domain, all variables denoted with the "–" and the "*" scripts become the actual variables, which also leads to zero DG2 operators in Eqs. (70) and (71). However, for completeness, the proof of Theorem 1 has been provided under the positivity-preserving reconstructions for the nodes, Eqs. (55)–(57), and their associated re-definition, Eqs. (58)–(60). It is worth mentioning that Eq. (57), needed for modifying the topography evaluations at the nodes, and Eqs. (58)–(60), needed for the definition of well-balanced modes under wetting and drying, are all necessary conditions for the scheme to overcome the challenges listed in Section 2.2.1.

To diagnostically explore the relevance of Eqs. (57)–(60), a highly irregular topography under a still water state is considered with wet–dry zones such that the following scenarios occur: (i) the wet–dry front is not located on a node where the topography is discretised (i.e. the local solution intersects a dry topography), (ii) the wet–dry front is exactly located on a node where the topography is discretised and (iii) the wet–dry front is associated with a water height equal to zero.

Therefore, a 1D test case is generated considering discontinuous terrain data over a 1D domain [0 m, 1500 m] [79], however with a smooth (hump-like) profile added to it and a still water condition of $h + z = 4$ m and $q_x = 0$ m^2/s, in order to simultaneously explore all three scenarios (i)-(iii). Figs. 3–5 illustrate simulated local DG2 linear solutions over a mesh of 50 computational cells and up $t = 50$ s. The results in Fig. 3 did not consider Eq. (57), whereas those in Fig. 4 did not consider Eqs. (58)–(61). Clearly, from these results the DG2 operators seem to only be (by $t = 20$ s and for certain portions) well-balanced under scenarios (ii) and (iii), though their full well-balancedness fall short under scenario (i). However, with Eqs. (57)–(60) active, as can be seen in Fig. 5, the DG2 operators remain well balanced for the full solution throughout the whole domain, i.e. under all scenarios (i)-(iii), and for a long time evolution.

2.2.3. Further considerations on well-balancedness in the 2D case

The 2D-DG2 operators in Eqs. (40)–(41) are reconsidered to study the well-balancedness for the planar solution (13) in light of the hypotheses made in Section 2.2.2. As in the 1D case, an appropriate initial projection, considering
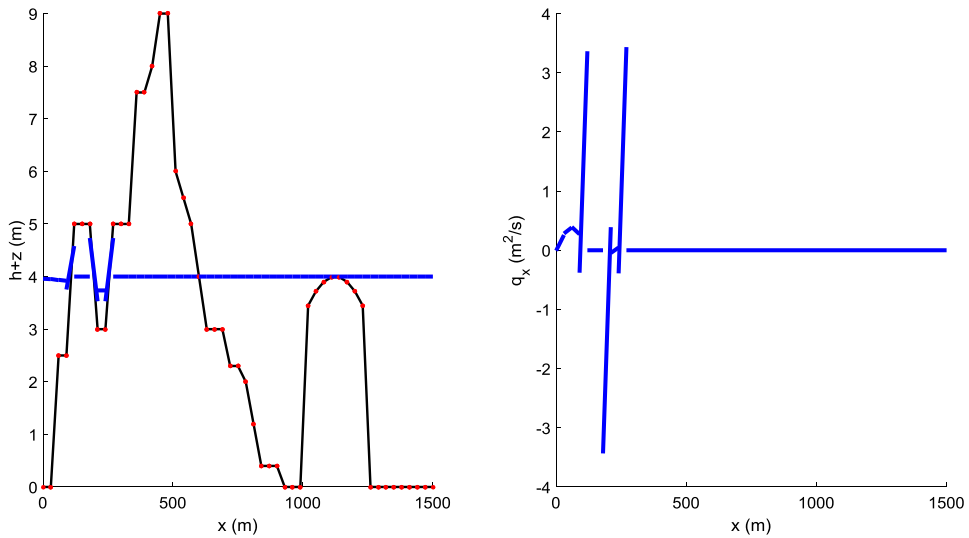
Fig. 4. Simulation (using 50 cells and up to 20 s) of a still water state for assessing the well-balancedness of operators (47)–(48) without considering conditions (58)–(61); "blue lines" = local linear DG2 flow solutions, "black lines" = local DG2 linear topography projections, "red markers" = nodal evaluations of the topography at interfaces. (For interpretation of the references to colour in this figure legend, the reader is referred to the web version of this article.)
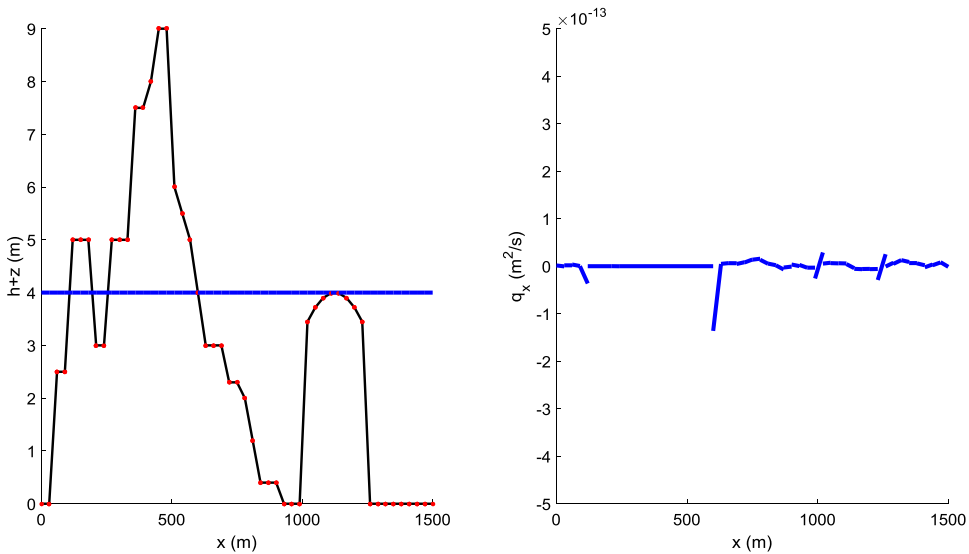
Fig. 5. Simulation (using 50 cells and up to 100 s) of a still water state for assessing the well-balancedness of operators (47)–(48) with condition (57)–(61) activated; "blue lines" = local linear DG2 flow solutions, "black lines" = local DG2 linear topography projections, "red markers" = nodal evaluations of the topography at interfaces. (For interpretation of the references to colour in this figure legend, the reader is referred to the web version of this article.)

the stencil in Fig. 2, is central for achieving the well-balancedness property. The initial conditions for the local coefficients in Eqs. (18)–(20) can be made valid on this stencil by involving the evaluations at the corner points EN, ES, WS, WN, as they are present in both stencils:

$$\mathbf{U}_c^0(0) = \frac{1}{4}\left[\mathbf{U_0}(EN) + \mathbf{U_0}(ES) + \mathbf{U_0}(WS) + \mathbf{U_0}(WN)\right] \tag{72}$$
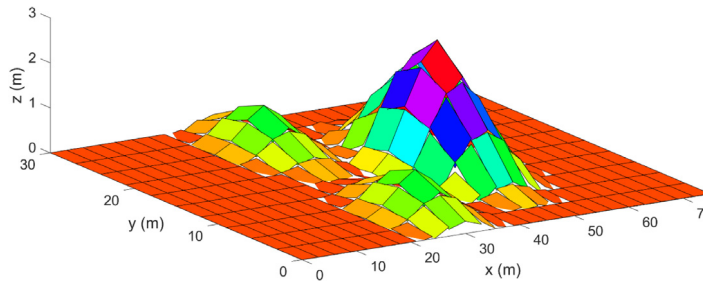
Fig. 6. 2D-DG2 planar projections $(z_h\,(x,\,y)\,|_{Q_c})_{Q_c}$ of a 2D topography function commonly reported in literature [68,72] — obtained via element-wise application of Eqs. (82) on a uniform mesh with square elements of size 3 m^2. As opposed to the 1D case, $(z_h\,(x,\,y)\,|_{Q_c})_{Q_c}$ cannot be globally continuous. However, via (79)–(81), they ensure continuity at the nodes E, W, N and S (see Fig. 2) where key treatments are performed.

$$\mathbf{U}_c^{1x}\,(0) = \frac{1}{4}\,[\mathbf{U_0}\,(EN) - \mathbf{U_0}\,(WN) + \mathbf{U_0}\,(ES) - \mathbf{U_0}\,(WS)] \tag{73}$$

$$\mathbf{U}_c^{1y}\,(0) = \frac{1}{4}\,[\mathbf{U_0}\,(EN) - \mathbf{U_0}\,(ES) + \mathbf{U_0}\,(WN) - \mathbf{U_0}\,(WS)] \tag{74}$$

In turn, given the slope-decoupled hypothesis, integrating over a coordinate direction the information at the faces considering the other direction are averaged, which leads to the following relationships:

$$\frac{1}{2}\,(\mathbf{U_0}\,(EN) + \mathbf{U_0}\,(ES)) = \mathbf{U_0}\,(E) \tag{75}$$

$$\frac{1}{2}\,(\mathbf{U_0}\,(WN) + \mathbf{U_0}\,(WS)) = \mathbf{U_0}\,(W) \tag{76}$$

$$\frac{1}{2}\,(\mathbf{U_0}\,(EN) + \mathbf{U_0}\,(WN)) = \mathbf{U_0}\,(N) \tag{77}$$

$$\frac{1}{2}\,(\mathbf{U_0}\,(WS) + \mathbf{U_0}\,(ES)) = \mathbf{U_0}\,(S) \tag{78}$$

By substituting Eqs. (75)–(78) into Eqs. (72)–(74), the initial conditions for the coefficients can be rewritten so that to involve the nodes E, W, N and S (see Fig. 2) where key treatments are performed:

$$\mathbf{U}_c^0\,(0) = \frac{1}{2}\,[\mathbf{U_0}\,(E) + \mathbf{U_0}\,(W)] = \frac{1}{2}\,[\mathbf{U_0}\,(N) + \mathbf{U_0}\,(S)] \tag{79}$$

$$\mathbf{U}_c^{1x}\,(0) = \frac{1}{2}\,[\mathbf{U_0}\,(E) - \mathbf{U_0}\,(W)] \tag{80}$$

$$\mathbf{U}_c^{1y}\,(0) = \frac{1}{2}\,[\mathbf{U_0}\,(N) - \mathbf{U_0}\,(S)] \tag{81}$$

Eqs. (79)–(81) provide an alternative option for initialising the average and slope coefficients of the local planar solution. However, their relevance becomes important when linking the modes to the *inter-elemental nodes* where flux exchange occurs, hence making them suited for altering the modes based on any change occurring at the nodes due to wetting and drying treatments, as seen in the 1D case. Also, Eqs. (79)–(81) reveal even more clearly that the planar topography projections, denoted by $z_h\,(x,\,y)\,|_{Q_c}$ over Q_c with coefficients z_c^0, z_c^{1x} and z_c^{1y} defined as in Eqs. (72)–(74), are *continuous at all four main nodes,* E, W, N and S, considering the stencil in Fig. 2, however without being necessarily continuous as in the 1D case. An illustrative example is given in Fig. 6, which shows the spatial 2D-DG2 planar projections, $\left(z_h\,(x,\,y)\,|_{Q_c}\right)_{Q_c}$, of 2D hump profiles based on Eqs. (72)–(74) where the continuity property only holds at all four central nodes located at an element's faces. Such property can be demonstrated by following a similar reasoning as in the 1D case (Eq. (51)–(53)).

Another key issue is how to evaluate the derivative of the local topography projections $\partial_x z_h|_{Q_c}$ and $\partial_y z_h|_{Q_c}$ while remaining consistent with the stencil in Fig. 2. A straightforward method would be to derive them from the following local planar solution, $z_h|_{Q_c}$:

$$z_h|_{Q_c} = z_h\,(x(\xi),\,y(\eta))\,|_{Q_c} = z_c^0 + \xi z_c^{1x} + \eta z_c^{1y} \tag{82}$$

which has constant slope coefficients over Q_c and thus leads to the following local bed slope terms:

$$\partial_x z_h|_{Q_c} = \left(\frac{2}{\Delta x}\right) z_c^{1x} \tag{83}$$

$$\partial_y z_h|_{Q_c} = \left(\frac{2}{\Delta y}\right) z_c^{1y} \tag{84}$$

Although counter-intuitive, the use of Eqs. (83)–(84) to discretise the local bed slope terms suffices to ensure well-balancedness for the average coefficients. However, this introduces irrelevant cross-dimensional slope dependencies (e.g. z_c^{1x} within L_c^{1y}) across the DG2 operators responsible for the update of slope coefficients (see proof of Theorem 2), leading to mild unbalancedness in the slope coefficients of the discharges, which might eventually impact the well-balancedness of all the coefficients (as shown later in Section 3.2.1). Therefore, an alternative slope-decoupled discretisation for the local bed gradients is here proposed:

$$\partial_x \left[z_h\left(0, y\right)|_{x=0}\right] = 0 \quad \text{and} \quad \partial_x z_h|_{y=0} = \partial_x \left[z_h\left(x, 0\right)|_{Q_c}\right] = \left(\frac{2}{\Delta x}\right) z_c^{1x} \tag{85}$$

$$\partial_y \left[z_h\left(x, 0\right)|_{y=0}\right] = 0 \quad \text{and} \quad \partial_y z_h|_{x=0} = \partial_y \left[z_h\left(0, y\right)|_{Q_c}\right] = \left(\frac{2}{\Delta y}\right) z_c^{1y} \tag{86}$$

In addition, to retain the well-balanced property in the presence of wetting and drying, the positivity-preserving amendments are applied at the nodes, as in the 1D case through Eqs. (55)–(57). By denoting with $\mathbf{U}_E^{\pm}$, $\mathbf{U}_W^{\pm}$, $\mathbf{U}_N^{\pm}$, and $\mathbf{U}_S^{\pm}$ the limits of the DG2 solutions at nodes E, W, N and S, that is:

$$\mathbf{U}_E^{\pm} = \mathbf{U}_h\left(E^{\pm}\right) = \left[h_E^{\pm}, (q_x)_E^{\pm}, \left(q_y\right)_E^{\pm}\right]^T \quad \text{and} \quad z_E = z_h(E^{\pm}) \tag{87}$$

$$\mathbf{U}_W^{\pm} = \mathbf{U}_h\left(W^{\pm}\right) = \left[h_W^{\pm}, (q_x)_W^{\pm}, \left(q_y\right)_W^{\pm}\right]^T \quad \text{and} \quad z_W = z_h(W^{\pm}) \tag{88}$$

$$\mathbf{U}_N^{\pm} = \mathbf{U}_h\left(N^{\pm}\right) = \left[h_N^{\pm}, (q_x)_N^{\pm}, \left(q_y\right)_N^{\pm}\right]^T \quad \text{and} \quad z_N = z_h(N^{\pm}) \tag{89}$$

$$\mathbf{U}_S^{\pm} = \mathbf{U}_h\left(S^{\pm}\right) = \left[h_S^{\pm}, (q_x)_S^{\pm}, \left(q_y\right)_S^{\pm}\right]^T \quad \text{and} \quad z_S = z_h(S^{\pm}) \tag{90}$$

their positivity-preserving reconstructions (following similar procedures as in Eqs. (55)–(57)) will be denoted by [64], $\{\mathbf{U}_E^{\pm,*}, z_E^*\}$, $\{\mathbf{U}_W^{\pm,*}, z_W^*\}$, $\{\mathbf{U}_N^{\pm,*}, z_N^*\}$ and $\{\mathbf{U}_S^{\pm,*}, z_S^*\}$. Eqs. (79)–(81) are then applied to re-define positivity-preserving modes based on the latter reconstructions, as follows:

$$\overline{\mathbf{U}}_c^{0x}(t) = \frac{1}{2}\left[\mathbf{U}_E^{-,*} + \mathbf{U}_W^{+,*}\right] \tag{91}$$

$$\overline{\mathbf{U}}_c^{0y}(t) = \frac{1}{2}\left[\mathbf{U}_N^{-,*} + \mathbf{U}_S^{+,*}\right] \tag{92}$$

$$\overline{\mathbf{U}}_c^{1x}(t) = \frac{1}{2}\left[\mathbf{U}_E^{-,*} - \mathbf{U}_W^{+,*}\right] \tag{93}$$

$$\overline{\mathbf{U}}_c^{1y}(t) = \frac{1}{2}\left[\mathbf{U}_N^{-,*} - \mathbf{U}_S^{+,*}\right] \tag{94}$$

It is worth noting that Eqs. (91) and (92) are identical so long as no change occur at any node due to wetting and drying. This decoupled form for the average coefficients is consistent with slope decoupling, and yet necessary to preserve well-balancedness for the slope coefficients when wetting and drying occur at any of the nodes E, W, N or S (Fig. 2). In addition to Eqs. (91)–(94), the bed gradient terms need to be re-defined in relation to potential change made by the wetting and drying at any of the nodes, as follows:

$$\overline{z}_c^{1x} = \frac{1}{2}\left[z_E^* - z_W^*\right] \tag{95}$$

$$\overline{z}_c^{1y} = \frac{1}{2}\left[z_N^* - z_S^*\right] \tag{96}$$

In the following, we demonstrate the well-balancedness property in the 2D case under consideration.

Theorem 2. *The proposed Eqs.* (91)–(96) *for the modes preceded by positivity-preserving reconstructions at the nodes, i.e.* $\{\mathbf{U}_E^{\pm,*}, z_E^*\}$, $\{\mathbf{U}_W^{\pm,*}, z_W^*\}$, $\{\mathbf{U}_N^{\pm,*}, z_N^*\}$ *and* $\{\mathbf{U}_S^{\pm,*}, z_S^*\}$, *yield well-balanced DG2 spatial operators in 2D provided that Eqs.* (85) *and* (86) *are used to incorporate the slopes coefficients of the topography in Eqs.* (95) *and* (96).

Proof. Under discrete still water conditions and after Eqs. (91)–(96), Eqs. (44) can be expressed as:

$$\bar{h}_c^{1x} + \bar{z}_c^{1x} = 0 \quad \text{and} \quad \bar{h}_c^{1y} + \bar{z}_c^{1y} = 0 \tag{97}$$

$$\bar{h}_c^{0x} = \frac{h_E^{-,*} + h_W^{+,*}}{2} \quad \text{and} \quad \bar{h}_c^{1x} = \frac{h_E^{-,*} - h_W^{+,*}}{2} \tag{98}$$

$$\bar{h}_c^{0y} = \frac{h_N^{-,*} + h_S^{+,*}}{2} \quad \text{and} \quad \bar{h}_c^{1y} = \frac{h_N^{-,*} - h_S^{+,*}}{2} \tag{99}$$

Now, the main variable is h_h, the mass conservation equation vanishes, and only hydrostatic balance equations remain within the momentum equations relative to both x- and y-directions.

Within these conditions, the fluxes and source terms involved in the momentum equations are:

$$\mathbf{F}(h_h) = \begin{bmatrix} \frac{g}{2}h_h^2 \\ 0 \end{bmatrix}, \mathbf{G}(h_h) = \begin{bmatrix} 0 \\ \frac{g}{2}h_h^2 \end{bmatrix}, \mathbf{S}(h_h) = \begin{bmatrix} -gh_h\partial_x z_h \\ -gh_h\partial_y z_h \end{bmatrix} \tag{100}$$

The difference and the sum of the Riemann fluxes become:

$$\tilde{\mathbf{F}}(h_E^{-,*}) - \tilde{\mathbf{F}}(h_W^{+,*}) = \frac{g}{2}\begin{bmatrix} \left(2\bar{h}_c^{0x}\right)\left(2\bar{h}_c^{1x}\right) \\ 0 \end{bmatrix} \tag{101}$$

$$\tilde{\mathbf{G}}(h_N^{-,*}) - \tilde{\mathbf{G}}(h_S^{+,*}) = \frac{g}{2}\begin{bmatrix} 0 \\ \left(2\bar{h}_c^{0y}\right)\left(2\bar{h}_c^{1y}\right) \end{bmatrix} \tag{102}$$

$$\tilde{\mathbf{F}}(h_E^{-,*}) + \tilde{\mathbf{F}}(h_W^{+,*}) = \frac{g}{2}\begin{bmatrix} 2\left(\bar{h}_c^{0x}\right)^2 + 2\left(\bar{h}_c^{1x}\right)^2 \\ 0 \end{bmatrix} \tag{103}$$

$$\tilde{\mathbf{G}}(h_N^{-,*}) + \tilde{\mathbf{G}}(h_S^{+,*}) = \frac{g}{2}\begin{bmatrix} 0 \\ 2\left(\bar{h}_c^{0y}\right)^2 + 2\left(\bar{h}_c^{1y}\right)^2 \end{bmatrix} \tag{104}$$

The volume integral of the flux term (involved in the slope evolution operators (41) and (42)) become:

$$\mathbf{F}(h_h(G_{x2})) + \mathbf{F}(h_h(G_{x1})) = \begin{bmatrix} \frac{g}{2}\left[2\left(\bar{h}_c^{0x}\right)^2 + \frac{2}{3}\left(\bar{h}_c^{1x}\right)^2\right] \\ 0 \end{bmatrix} \tag{105}$$

$$\mathbf{G}(h_h(G_{x2})) + \mathbf{G}(h_h(G_{x1})) = \begin{bmatrix} 0 \\ \frac{g}{2}\left[2\left(\bar{h}_c^{0y}\right)^2 + \frac{2}{3}\left(\bar{h}_c^{1y}\right)^2\right] \end{bmatrix} \tag{106}$$

The source term evaluations involved in the evolution operators (40)–(42) become, if considering a standard planar discretisation as per (83) and (84):

$$\mathbf{S}(h_h(x_c)) = \begin{bmatrix} -g\bar{h}_c^{0x}\left(\dfrac{2\bar{z}_c^{1x}}{\Delta x}\right) \\ -g\bar{h}_c^{0y}\left(\dfrac{2\bar{z}_c^{1y}}{\Delta y}\right) \end{bmatrix} \tag{107}$$

$$\mathbf{S}(h_h(G_{x2})) - \mathbf{S}(h_h(G_{x1})) = \begin{bmatrix} -g\left(\dfrac{2\bar{z}_c^{1x}}{\Delta x}\right)\left(\dfrac{\bar{h}_c^{1x}}{\sqrt{3}}\right) \\ -g\left(\dfrac{2\bar{z}_c^{1y}}{\Delta y}\right)\left(\dfrac{\bar{h}_c^{1x}}{\sqrt{3}}\right) \end{bmatrix} \tag{108}$$

$$\mathbf{S}\left(h_h\left(G_{y2}\right)\right) - \mathbf{S}\left(h_h\left(G_{y1}\right)\right) = \begin{bmatrix} -g\left(\dfrac{2\bar{z}_c^{1x}}{\Delta x}\right)\left(\dfrac{\bar{h}_c^{1y}}{\sqrt{3}}\right) \\ -g\left(\dfrac{2\bar{z}_c^{1y}}{\Delta y}\right)\left(\dfrac{\bar{h}_c^{1y}}{\sqrt{3}}\right) \end{bmatrix} \tag{109}$$

Replacing Eqs. (101)–(109) in Eqs. (40)–(42), considering only the remaining terms in the momentum conservation equation, the DG2 operators can be rearranged as follows:

$$\mathbf{L}_c^0 = \begin{bmatrix} -\dfrac{2g}{\Delta x}\left[\bar{h}_c^{0x}\left(\bar{h}_c^{1x} + \bar{z}_c^{1x}\right)\right] \\ -\dfrac{2g}{\Delta y}\left[\bar{h}_c^{0y}\left(\bar{h}_c^{1y} + \bar{z}_c^{1y}\right)\right] \end{bmatrix} \tag{110}$$

$$\mathbf{L}_c^{1x} = \begin{bmatrix} -\dfrac{3g}{\Delta x}\left\{\dfrac{2}{3}\left(\bar{h}_c^{1x}\right)^2 - \dfrac{2}{3}\left[\left(-\bar{z}_c^{1x}\right)\left(\bar{h}_c^{1x}\right)\right]\right\} \\ -\dfrac{g}{\Delta y}\left(\bar{z}_c^{1y}\bar{h}_c^{1x}\right) \end{bmatrix} \tag{111}$$

$$\mathbf{L}_c^{1y} = \begin{bmatrix} -\dfrac{g}{\Delta x}\left(\bar{z}_c^{1x}\bar{h}_c^{1y}\right) \\ -\dfrac{3g}{\Delta y}\left\{\dfrac{2}{3}\left(\bar{h}_c^{1y}\right)^2 - \dfrac{2}{3}\left[\left(-\bar{z}_c^{1y}\right)\left(\bar{h}_c^{1y}\right)\right]\right\} \end{bmatrix} \tag{112}$$

By also applying the slope conditions in Eqs. (97), i.e. $-\bar{z}_c^{1x} = \bar{h}_c^{1x}$ and $-\bar{z}_c^{1y} = \bar{h}_c^{1y}$, Eqs. (110)–(112) are simplified to:

$$\mathbf{L}_c^0 = \begin{bmatrix} 0 \\ 0 \end{bmatrix} \tag{113}$$

$$\mathbf{L}_c^{1x} = \begin{bmatrix} 0 \\ \dfrac{g}{\Delta y}\left(\bar{z}_c^{1y}\bar{z}_c^{1x}\right) \end{bmatrix} \tag{114}$$

$$\mathbf{L}_c^{1y} = \begin{bmatrix} \dfrac{g}{\Delta x}\left(\bar{z}_c^{1x}\bar{z}_c^{1y}\right) \\ 0 \end{bmatrix} \tag{115}$$

Clearly, Eqs. (113)–(115) show that only operator $\mathbf{L}_c^0$ vanishes, meaning that the scheme is well-balanced only for the average (discharge) coefficients. As for the (discharge) slope coefficients, well-balancedness is partially met given the remaining cross-dimensional slope dependency introduced in $\mathbf{L}_c^{1x}$ and $\mathbf{L}_c^{1y}$ by using (83) and (84) to discretise the local bed slope terms.

Therefore, to have the slope-decoupled DG2 operators well-balanced in full, the discretisation in Eqs. (85) and (86) must be considered instead prior to evaluating Eqs. (108) and (109), leading to the following slope-decoupled versions of them:

$$\mathbf{S}\left(h_h\left(G_{x2}\right)\right) - \mathbf{S}\left(h_h\left(G_{x1}\right)\right) = \begin{bmatrix} -g\left(\dfrac{2\bar{z}_c^{1x}}{\Delta x}\right)\left(\dfrac{\bar{h}_c^{1x}}{\sqrt{3}}\right) \\ 0 \end{bmatrix} \tag{116}$$

$$\mathbf{S}\left(h_h\left(G_{y2}\right)\right) - \mathbf{S}\left(h_h\left(G_{y1}\right)\right) = \begin{bmatrix} 0 \\ -g\left(\dfrac{2\bar{z}_c^{1y}}{\Delta y}\right)\left(\dfrac{\bar{h}_c^{1y}}{\sqrt{3}}\right) \end{bmatrix} \tag{117}$$

In turn, Eqs. (116) and (117) – together with (101)–(107) in (40)–(42) – lead to full zeroing of the DG2 slope operators $\mathbf{L}_c^{1x}$ and $\mathbf{L}_c^{1y}$, as needed to ensure fully well-balanced DG2 planar solutions and slope-decoupled 2D-DG2 scheme.

3. Numerical tests

In this section, numerical results for selected 2D test cases are presented to compare the slope-decoupled DG2 form with the standard DG2 form, and verify its conservation properties for practical shallow water modelling. Section 3.1
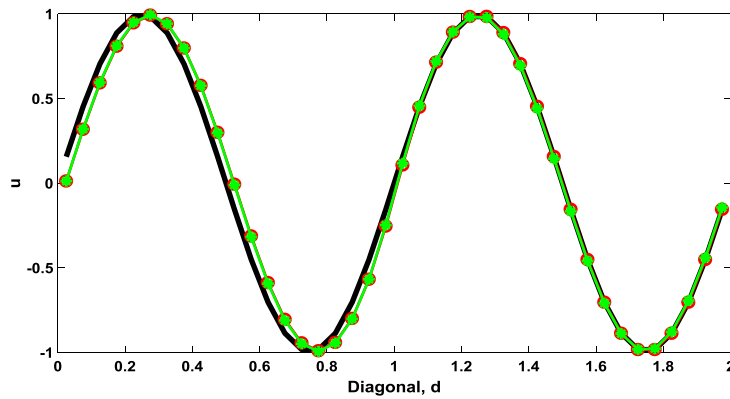
Fig. 7. Numerical results of the exact (black line), the standard DG2 scheme (red-dotted line) and the slope-decoupled DG2 scheme (green-dotted line) along the diagonal (using 40×40 cells). (For interpretation of the references to colour in this figure legend, the reader is referred to the web version of this article.)

contains a comparative investigation on the accuracy of the slope-decoupled DG2 scheme against the standard version based on classical benchmark tests (the linear advection and the radial dam-break tests). Section 3.2 explores the conservative properties of the slope-decoupled DG2 scheme (well-balancedness, total energy and accuracy) with test cases involving uneven topographies and wetting and drying processes. For both schemes, explicit adaptive time stepping is used based on a Courant–Friedrichs–Lewy (CFL) number equal to 0.25, and limiting of the slope-coefficients is restricted to when the shock detector in [53] exceeds the threshold 100.

3.1. Standard DG2 scheme vs. slope-decoupled DG2 scheme

The standard and slope-decoupled 2D-DG2 schemes are here benchmarked and compared against analytical or reference data. Two numerical 2D tests are considered involving bi-directional flows in order to entirely investigate the 2D character of the schemes. Quantitative analyses are conducted to investigate the mesh convergence rate of the DG2 schemes for the case of the 2D inviscid linear advection equation. A qualitative assessment of the schemes' ability in reproducing wave nonlinearities and discontinuities relevant to a classical radial dam-break flow is also provided.

3.1.1. Quantitative assessment

To generally compare the performance of the standard and slope-decoupled DG2 schemes, a 2D linear advection equation [10] is considered, which is usually the *model equation* on which numerical methods solving hyperbolic conservation laws were initially developed [10]:

$$\partial_t u + a\partial_x u + b\partial_y u = 0 \tag{118}$$

Eq. (118) is solved over a 2D domain $[0, 2]^2$ with characteristic speed coefficient $a = b = 1$. The initial condition is $u(x, y, 0) = sin(\pi(x + y))$ and boundary conditions are set to be periodic. Simulations are run up to $t = 1$ s on a series of quadrilateral meshes of $M \times N = 10 \times 10, 20 \times 20, 40 \times 40, 80 \times 80$ and 160×160 cells, respectively.

Fig. 7 illustrates the average coefficients produced by the standard and slope-decoupled DG2 schemes extracted diagonally from the mesh inclosing 40×40 cells and at $t = 1$ s. Both schemes appear to consistently predict the undulant characteristics observed in the analytical solution. Fig. 8 displays the local 2D planar solutions (i.e. via Eq. (13)) associated with both scheme predictions, showing a similar qualitative behaviour despite the difference in the stencils involved. To compare the schemes based on quantitative metrics, an accuracy-order and runtime cost analyses are performed. Table 1 contains the relative errors between the analytical and numerical solutions taken along the diagonal centreline, namely $Error = (1/MN)\|u_{\text{exact}} - u_{\text{DG2}}\|/\|u_{\text{exact}}\|$, which are evaluated considering the standard L^1-norm, L^2-norm and L^∞-norm. These errors are calculated for both the standard and the slope-decoupled DG2 schemes based on the aforementioned series of meshes, together with their respective rate of convergence and CPU runtimes, which are also included in Table 1. It can be observed in the table that the L^1-, L^2- and L^∞-errors of the
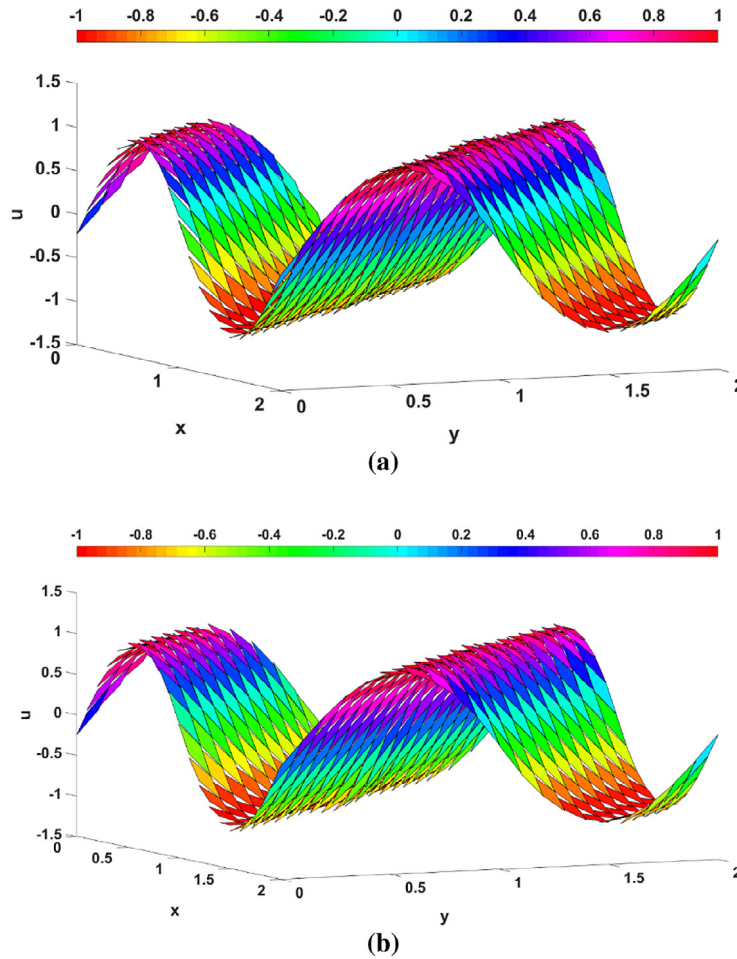
Fig. 8. The 2D full planar solutions $(u_h(x, y, t = 1s)|_{Q_c})_{Q_c}$ for the (a) standard DG2 scheme and (b) slope-decoupled scheme for the 20×20 cells domain.

Table 1
L^1-norm, L^2-norm and L^∞-norm errors and orders of accuracy of the standard and slope-decoupled DG2 schemes and their CPU times (relevant to the test in Section 3.1.1).

DG2 form	Mesh	L^1-error	L^1-order	L^2-error	L^2-order	L^∞-error	L^∞-order	Runtime
	10×10	$3.86E^{-02}$	–	$4.11E^{-02}$	–	$5.98E^{-02}$	–	4.0 s
	20×20	$8.70E^{-03}$	2.148	$1.03E^{-02}$	1.993	$1.53E^{-02}$	1.963	15.9 s
Standard	40×40	$2.00E^{-03}$	2.153	$2.50E^{-03}$	2.020	$3.60E^{-03}$	2.071	62.5 s
	80×80	$4.68E^{-04}$	2.067	$6.02E^{-04}$	2.081	$8.57E^{-04}$	2.090	243.6 s
	160×160	$1.17E^{-04}$	2.001	$1.34E^{-04}$	2.167	$1.93E^{-04}$	2.153	960.0 s
	10×10	$4.97E^{-02}$	–	$5.22E^{-02}$	–	$7.41E^{-02}$	–	1.8 s
	20×20	$1.00E^{-02}$	2.311	$1.20E^{-02}$	2.116	$1.74E^{-02}$	2.089	6.5 s
Slope-decoupled	40×40	$2.10E^{-03}$	2.268	$2.70E^{-03}$	2.130	$3.90E^{-03}$	2.151	24.5 s
	80×80	$4.87E^{-04}$	2.095	$6.22E^{-04}$	2.145	$8.92E^{-04}$	2.136	97.0 s
	160×160	$1.21E^{-04}$	2.003	$1.38E^{-04}$	2.170	$1.97E^{-04}$	2.176	381.8 s

slope-decoupled DG2 scheme are consistently slightly larger than those of the standard DG2 scheme. This clearly indicates that the slope-decoupled DG2 version is, as expected, slightly less accurate than the standard DG2 scheme. Nonetheless, looking at rate of convergence in Table 1 in terms of L^1-, L^2- and L^∞-orders, the slope-decoupled DG2 scheme can deliver second-order accurate predictions, which are practically as good as the standard DG2 scheme and, in this respect, constitutes a formally second-order accurate alternative. It is worth stating that consistent error and

accuracy-order results are obtainable by considering the full 2D profiles of the analytical and numerical solutions, instead of the 1D diagonal centreline, but were not illustrated here to save space. In terms of speed up ratio between the two DG2 schemes, the CPU runtimes in Table 1 indicate a range between 2.25 and 2.55, which is pretty close to the predicted operational cost ratio of 2.6 (Section 2.2).

3.1.2. Qualitative assessment

To further quantitatively compare the performances of the DG2 schemes in shallow water applications, a circular dam-break test [11] is here considered. Such test is appropriate for testing the schemes' ability to simulate shock propagating and rarefaction waves as it considers the instantaneous collapse of a circular dam on a flat bed. Water in the dam is contained by a thin 2.5 m radius circular wall centred at $x_c = 0$ m, $y_c = 0$ m. The water depth is 2.5 m inside the dam and 0.5 m outside. The model is a 40 m × 40 m square domain made up of 201 × 201 quadrilateral cells. Initial velocities u (along x) and v (along y) are set equal to zero and slip numerical boundary conditions are used. The reference solution [11] is obtained using a 1D second-order MUSCL finite volume solver [40] of the 1D radial-symmetric version of the 2D SWE on a mesh with 1001 cells. Fig. 9 shows the free surface elevation and velocity plots in the radial direction for the reference solution, the standard DG2 scheme and the slope-decoupled DG2 scheme. Immediately after the initial collapse of the dam, a primary shock wave began to propagate away from the centre, while a rarefaction wave moves inwardly and reaches the centre at $t = 0.4$ s (Fig. 9a) with a well-defined depth gradient developed behind the shock wave. At $t = 0.7$ s (Fig. 9b), the rarefaction wave has fully imploded at the centre and reflects radially outward, creating a small dip in the free surface where the velocity is nearing zero. At $t = 1.4$ s (Fig. 9c), the primary shock wave continues to move away from the centre and the free surface has dropped below the initial water depth outside of the dam. A secondary shock wave has also formed at this time, as clearly shown by the velocity profile, which exhibits two small and yet sharp fronts behind the primary shocks. At $t = 3.5$ s (Fig. 9d), the primary shock is approaching the boundary while the secondary shock is travelling in the opposite direction with the free surface falling very close to the bed. Finally, at $t = 4.7$ s (Fig. 9e), the primary shock is about to reach the boundary while the secondary shock has imploded in the centre and reflects outwardly, resulting in another dip in the free surface at the centre.

As seen in Fig. 9a, at $t = 0.4$ s, the standard DG2 scheme satisfactorily corresponds with the reference solution, except at the peak free surface elevation associated with local zero velocities. There, it shows a slight overestimation as compared to the slope-decoupled DG2 version. This seems to indicate that the standard DG2 scheme is much more sensitive to slope variations around points of critical flow. The discrepancy between the two DG2 schemes is also due to the convoluted involvement of both directional slope-coefficients combined with the over-allowing character of the shock detector adopted for local limiting. In other words, its overlooking effects (to reduce the applicability of the *minmod* slope limiter) are expected to double when applied with the standard DG2 scheme. However, such discrepancy does not affect the overall performance of the scheme, as one may observe in the predictions at $t = 0.7$ s and $t = 1.4$ s (Fig. 9b and c). At these times, the flow only entails primary waves and both DG2 schemes provide predictions very similar to the reference solutions. When the secondary waves emerge at $t = 3.5$ s and $t = 4.7$ s (Fig. 9d and e), the predictive capability of the standard DG2 and the slope-decoupled DG2 schemes becomes more distinct in the results, especially around the flow features defined by the secondary shock fronts and associated pattern where the standard version clearly outperforms. However, the slope-decoupled DG2 scheme still delivers 2D predictions that are close to those achieved by the standard DG2 scheme, and can satisfactory trail the sequence and form of the shock and rarefaction waves produced by the reference solutions.

3.2. Verification of scheme properties

The previous tests have shown that the slope-decoupled DG2 scheme is formally second-order accurate and able to capture complex wave propagations with predictive accuracy quite similar to the standard DG2 scheme. Here, the ability of the slope-decoupled DG2 scheme in preserving numerical conservation properties is further assessed. This involves 2D numerical tests aimed to assess the well-balancedness ability of the scheme for various scenarios involving smooth and sharp-edged terrain shapes with presence of wet–dry zones in the domain, and to conserve total energy and accuracy-order when the flow is subjected to constantly moving of wet–dry fronts over non-flat topography.

3.2.1. Well-balancedness

The first numerical test intends to diagnostically investigate the effects of the different DG2 based bed slope terms discretisation, i.e. Eqs. (83) and (84) *vs*. Eqs. (85) and (86), on the reliability of the slope-decoupled DG2 scheme in
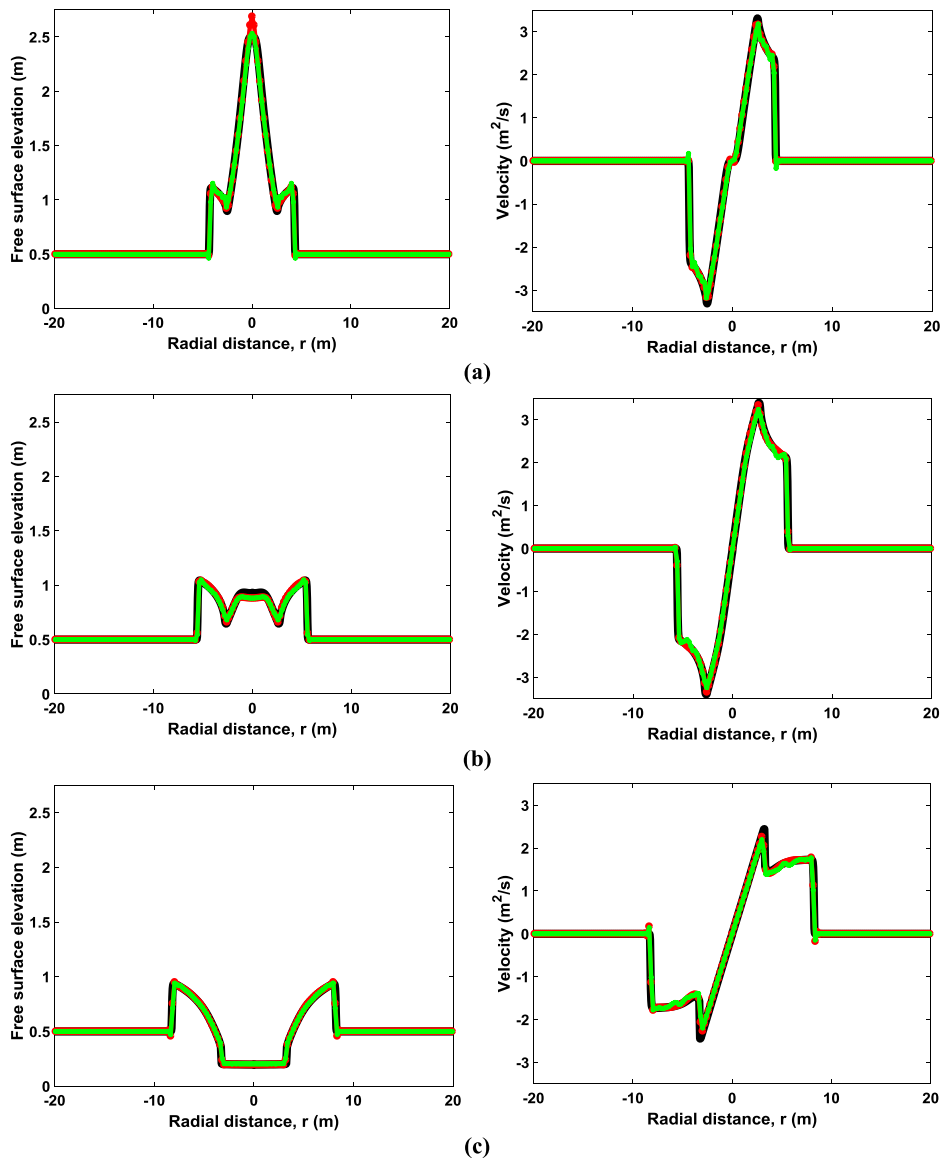
Fig. 9. The free surface elevation and velocity plots for the reference (black line), standard DG2 scheme (red line) and slope-decoupled DG2 scheme (green line) for (a) $t = 0.4$ s, (b) $t = 0.7$ s, (c) $t = 1.4$ s, (d) $t = 3.5$ s, and (e) $t = 4.7$ s. (For interpretation of the references to colour in this figure legend, the reader is referred to the web version of this article.)

numerically preserving the well-balanced property over uneven terrain with wetting and/or drying. The test assumes a motionless flow in a 75 m × 30 m domain. Two cases are investigated to distinguish between differential and non-differential topography shapes, which resemble real-world natural and artificial terrain features. The differential topography represents a hilly terrain and consists of three mounds with different peak heights. In such case, the topography function is:

$$z(x, y) = max\left[0, 1 - \frac{1}{5}\sqrt{(x - 20)^2 + (y - 15)^2}, 2 - \frac{1}{2}\sqrt{(x - 40)^2 + (y - 15)^2},\right.$$

$$\left. 3 - \frac{3}{10}\sqrt{(x - 60)^2 + (y - 15)^2}\right]$$

$$(119)$$

(d)

(e)
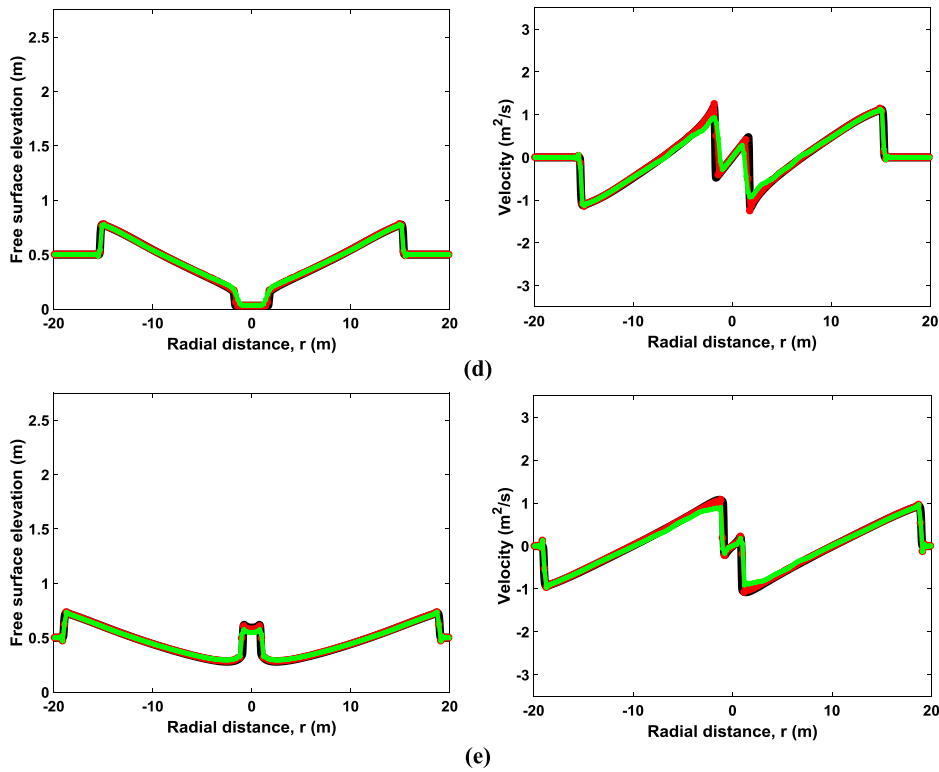
Fig. 9. (*continued*)

Alternatively, the non-differential topography resembles buildings of varying heights and consists of three rectangular blocks. In this other case, the topography function is:

$$z(x, y) = \begin{cases} 0.86 & if \ 16 \le x \le 24, 11 \le y \le 19 \\ 1.78 & if \ 36 \le x \le 44, 11 \le y \le 19 \\ 2.30 & if \ 56 \le x \le 64, 11 \le y \le 19 \\ 0 & otherwise \end{cases} \tag{120}$$

Fig. 10(a) and (b) provide a view on the 2D local planar DG2 projections, via Eq. (82), for the topography functions (119) and (120), respectively. In both cases, the choice for the initial free-surface elevation is taken according to three scenarios: fully submerged ($h > 0$ m at one peak), critically wet ($h = 0$ m at another peak) and partially wet involving wet–dry fronts ($h < 0$ m, in the sense where the local planar DG2 solutions cut through the highest peak). This leads to set a free-surface elevation value of 1.78 m and 1.95 m for the first and second cases, respectively (see also Fig. 10) together with zero discharge values for q_x and q_y. These initial states should be maintained as there is no external force exerted on the flow at any of the boundaries. To study the numerical well-balancedness of the slope-decoupled DG2 scheme, the domain is discretised using quadrilateral 1 m^2 cells, and simulations are run for relatively long time evolution ($t = 100$ s) considering transmissive numerical boundary conditions. To conduct a thorough analysis of well-balancedness, the time histories of the maximum errors are calculated (for each simulation) for all the discharge coefficients spanning the local DG2 solutions (namely the average coefficients q_x^0 and q_y^0, the x-directional slope coefficients q_x^{1x} and q_y^{1x}, and the y-directional slope coefficients q_x^{1y} and q_y^{1y}). These errors are plotted and analysed to explore the well-balancedness *at the level of both the average- and the slope-coefficients*.

Simulation results relative to the first case are summarised in Fig. 11, which shows time series of the errors for the average and slope (discharge) coefficients up to $t = 100$ s. In particular, Fig. 11(a) shows the results considering the bed slope discretisation in Eqs. (83) and (84). At the start of the simulation ($t < 7$ s), the average coefficients q_x^0
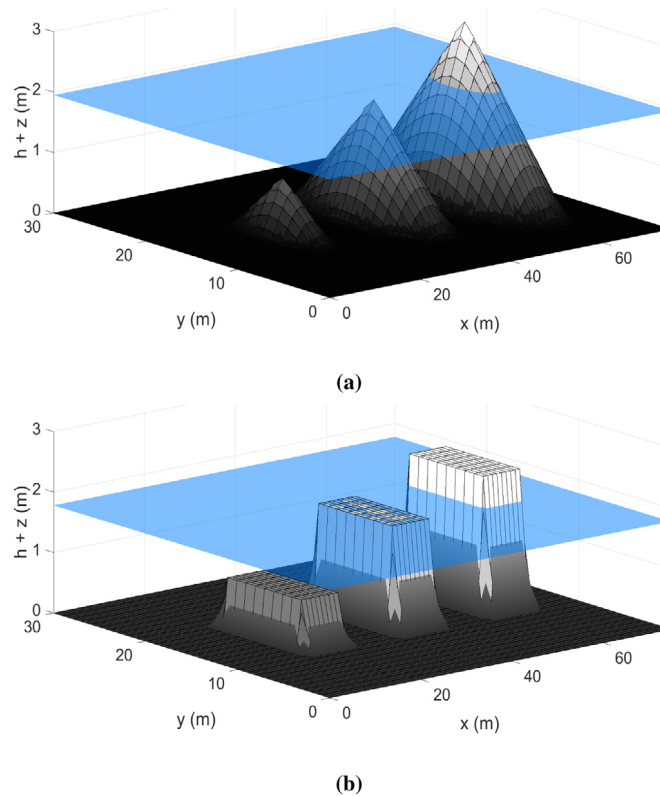
Fig. 10. The initial water surface and full planar DG2 topography projections $(z_h\,(x,y)\,|_{Q_c})_{Q_c}$, via (82), of: (a) differential topography (119) and (b) non-differential topography (120).

and q_y^0 are within the round-off error even in the presence of wet–dry fronts. This finding reinforces the statement within Theorem 2, according to which the scheme should be well-balanced for the means with both bed slope term discretisations Eqs. (83) and (84) and (85) and (86). In Fig. 11a, similar behaviour can also be observed for the discharge slope coefficients relative to the mainstream directions, q_x^{1x} and q_y^{1y}. However, the discharge slope coefficients across the opposite direction, q_x^{1y} and q_y^{1x}, display a different behaviour, showing a drastic rise in error magnitudes from the very start of the simulation. Although this rise seems to settle quite soon ($t > 17$ s), it appears to produce numerical artefacts, which gradually (for $t > 7$ s) affect the other discharge coefficients, initially well-balanced (for $t < 7$ s). From $t = 17$ s onward, relatively mild perturbations are observed for all discharge coefficients, which seems to suggest that Eqs. (83) and (84) do not provide a fully well-balanced slope-decoupled DG2 scheme. In contrast, by re-running the simulation using the proposed alternative topography discretisation, via Eqs. (85) and (86), more consistent error magnitudes are obtained as shown in Fig. 11(b). In this setting, it can be noticed that the variation of all discharge coefficient errors remains substantially bounded within the range of the round-off throughout the simulation.

In the second case, where the topography function is not differentiable, the adverse effects of the choice of the bed slope discretisation of Eqs. (83) and (84) are observed to augment as seen in Fig. 12(a). The resulting time series for the discharge coefficient (maximum) errors again imply a partially well-balanced behaviour up to certain time around $t = 13$ s, i.e. for the average coefficients, q_x^0 and q_y^0, and the slope coefficients relative to the mainstream directions, q_x^{1x} and q_y^{1y}. However, the errors produced for the cross-directional slope coefficients, q_x^{1y} and q_y^{1x}, are now seen to exhibit a much higher increase up to eight times larger than those observed in the first case (compare Figs. 11(a) to 12(a)). These errors continue to rise until $t = 13$ s when they reduce and become relatively stable. They also show a behaviour similar to the first case, in that they eventually (13 s $< t <$ 100 s) affect the errors of the other discharge coefficients, which were initially well-balanced (0 s $< t <$ 13 s). These findings seem to suggest
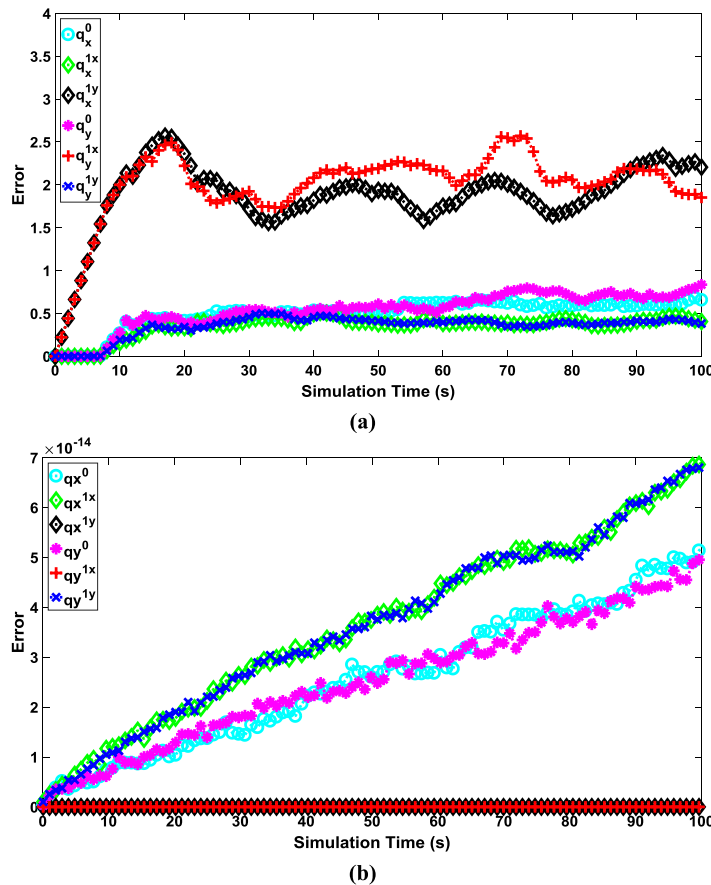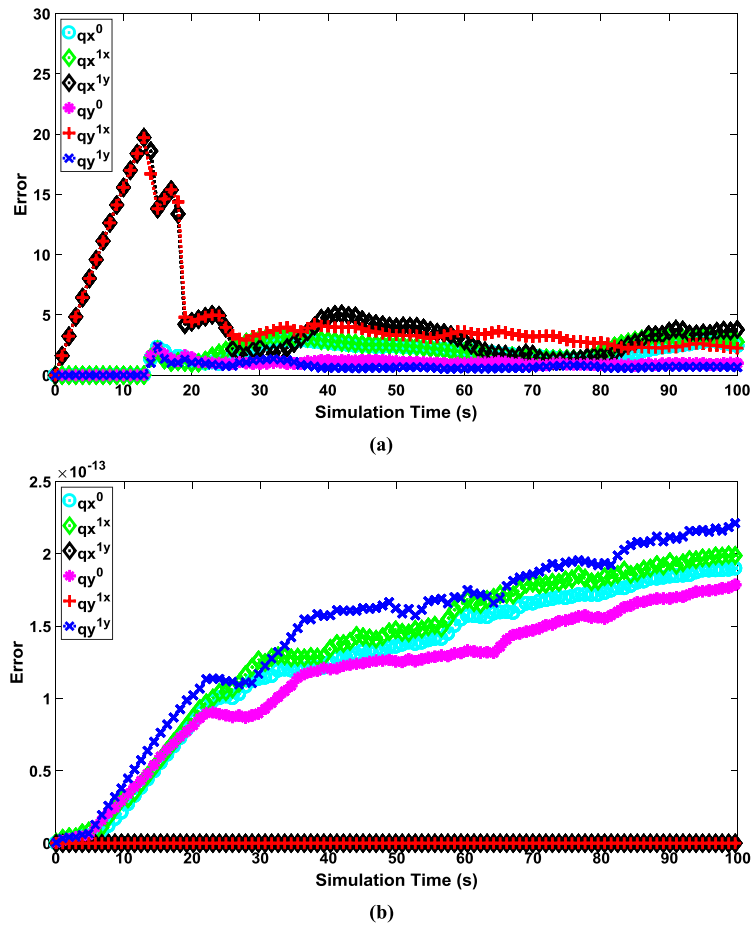
Fig. 11. Time series of the resulting maximum errors for the average and slope discharge coefficients over a differential topography (case 1) using the (a) original discretisation Eqs. (83) and (84)and (b) alternative discretisation Eqs. (85) and (86).

that any unbalance in a slope coefficient, if overlooked, can gradually affect the well-balancedness property for all other coefficients, and hence eventually that of the full DG2 planar solutions. In contrast, by using the proposed choice for the bed slope term discretisation, via Eqs. (85) and (86), in combination with the slope-decoupled DG2 scheme all error magnitudes remain bounded near the range of machine precision, as shown in Fig. 12(b), irrespective of the discontinuous character of the topographies involved in this case. These results imply that all average and slope coefficients for the discharge remain numerically well-balanced in this setting. Hence, one can conclude that the slope-decoupled DG2 scheme complemented with Eqs. (85) and (86) for the bed slope discretisations is fully well-balanced for both mean- and slope-coefficients in all three scenarios.

3.2.2. Total energy and accuracy-order

Having verified that the slope-decoupled DG2 scheme with Eqs. (85) and (86) is well-balanced, further assessments are made to test the conservative features of this scheme. In particular, we verify numerical accuracy and total energy for a transient flow case involving moving 2D wet–dry fronts over a non-flat topography. This numerical test relies upon the well-known 2D oscillatory flow in a parabolic bowl problem [65], in which a set of parametric values are used following [64]. The model is set in a 2D domain of square length $[-4000, +4000 \text{ m}]^2$. The topography is defined as $z(x, y) = \alpha r^2$, where α is a constant equal to $1.6 \times 10^{-7} \text{ m}^{-1}$ and r is the radial distance $r^2 = \sqrt{x^2 + y^2}$. The initial velocities, $u(x, y, 0)$ and $v(x, y, 0)$, are set to zero, and the initial free surface elevation is $h(r, 0) = (1 + a(Y - X)r^2)/(X + Y)$, where X and Y are equal to 1 m^{-1} and -0.41884 m^{-1}, respectively. The wet domain is such that $h(r, t) > 0$ for $r < \sqrt{(X + Y \cos \omega t)/\alpha (X^2 - Y^2)}$, which can be used to identify the interface between the wet and dry regions. This numerical test assumes a period of $\tau = 2\pi/\omega$ equivalent to 1756.2 s

Fig. 12. Time series of the resulting maximum errors for the average and slope discharge coefficients over a non-differential topography (case 2) using the (a) original discretisation Eqs. (83) and (84) and (b) alternative discretisation Eqs. (85) and (86).

with $\omega^2 = 8g\alpha$. There is no specific boundary condition to be specified, as the free surface does not reach the domain boundary. The analytical solution is given in [80]:

$$h(r, t) = \frac{1}{X + Y\cos\omega t} + \alpha \left(Y^2 - X^2\right) \frac{r^2}{(X + Y\cos\omega t)^2} \tag{121}$$

$$(u(x, y, t), v(x, y, t)) = -\frac{Y\omega\sin\omega t}{X + Y\cos\omega t} \left(\frac{x}{2}, \frac{y}{2}\right) \tag{122}$$

Figs. 13 and 14 contain the plots of the computed free surface elevation and discharges, respectively, using similar mesh sizes and display patterns as in [65]. These figures allow to compare the average coefficients (or mean values) calculated by the selected DG2 scheme (across the centreline $x = 0$) with the exact solution for two meshes (i.e. $\Delta x = 100$ and 200) at the six output times $t = 0, \tau/6, 2\tau/6, 3\tau/6, 4\tau/6, 5\tau/6$ and τ. In the prediction of the free surface elevation, as shown in Fig. 13, the current DG2 scheme is observed to perform very well, yielding calculations that are in good agreement with the exact solutions for all the output times considered, and irrespective of the meshes spacing. Fig. 14 shows that, in terms of discharge predictability the scheme is also observed to closely trail the exact profiles for both meshes and at almost all output times, except at $t = \tau$ when the numerical solutions do not fully capture the zero discharge, which is a common deficiency for this test [41,64,65]. Generally, these results reveal that the present slope-decoupled DG2 scheme can capture flow features with curvature and persistent wetting and drying.
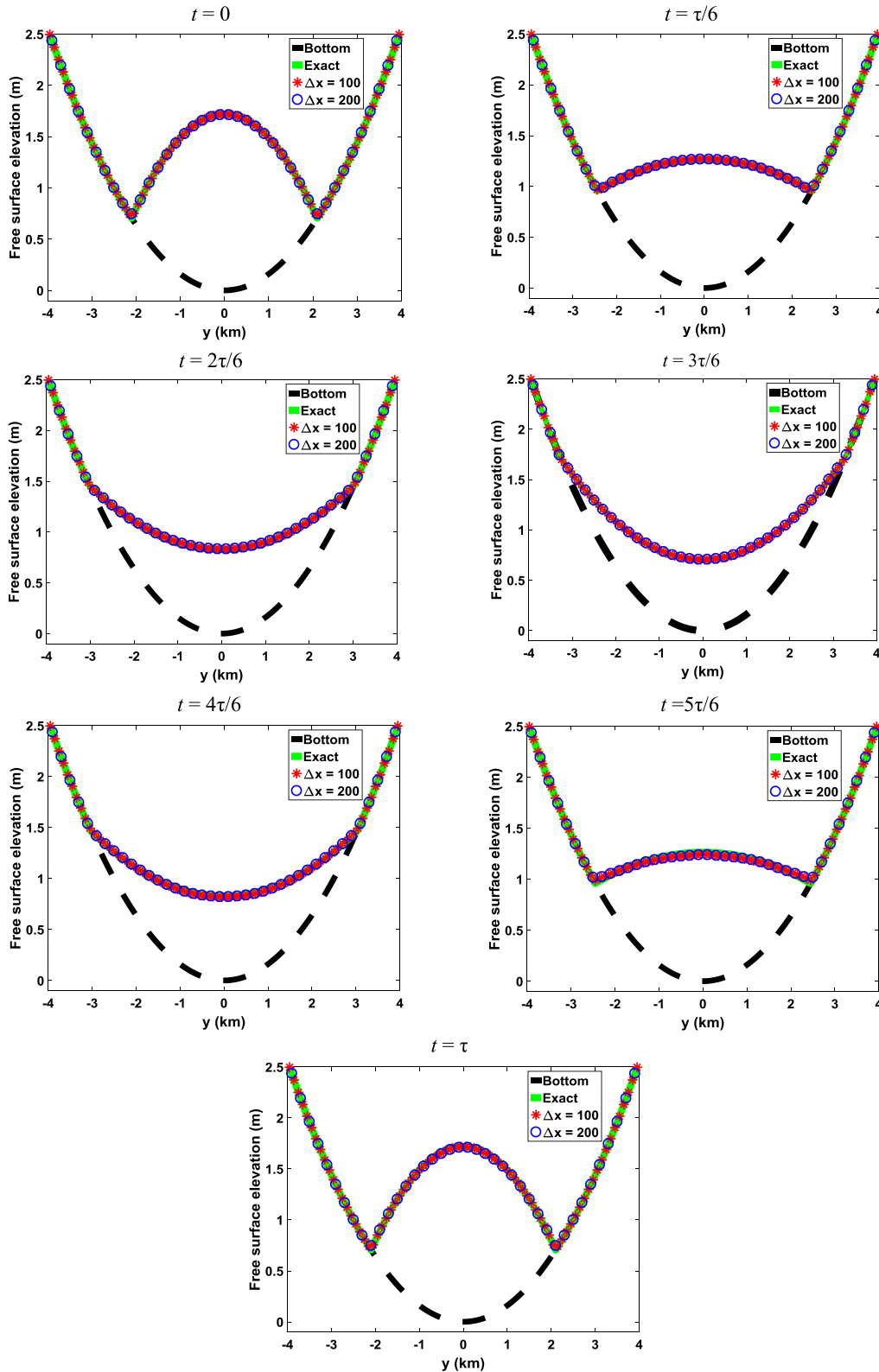
Fig. 13. Free surface elevation sliced along $x = 0$ at six output times considering two mesh resolutions with cell size $\varDelta x = 100$ and 200.
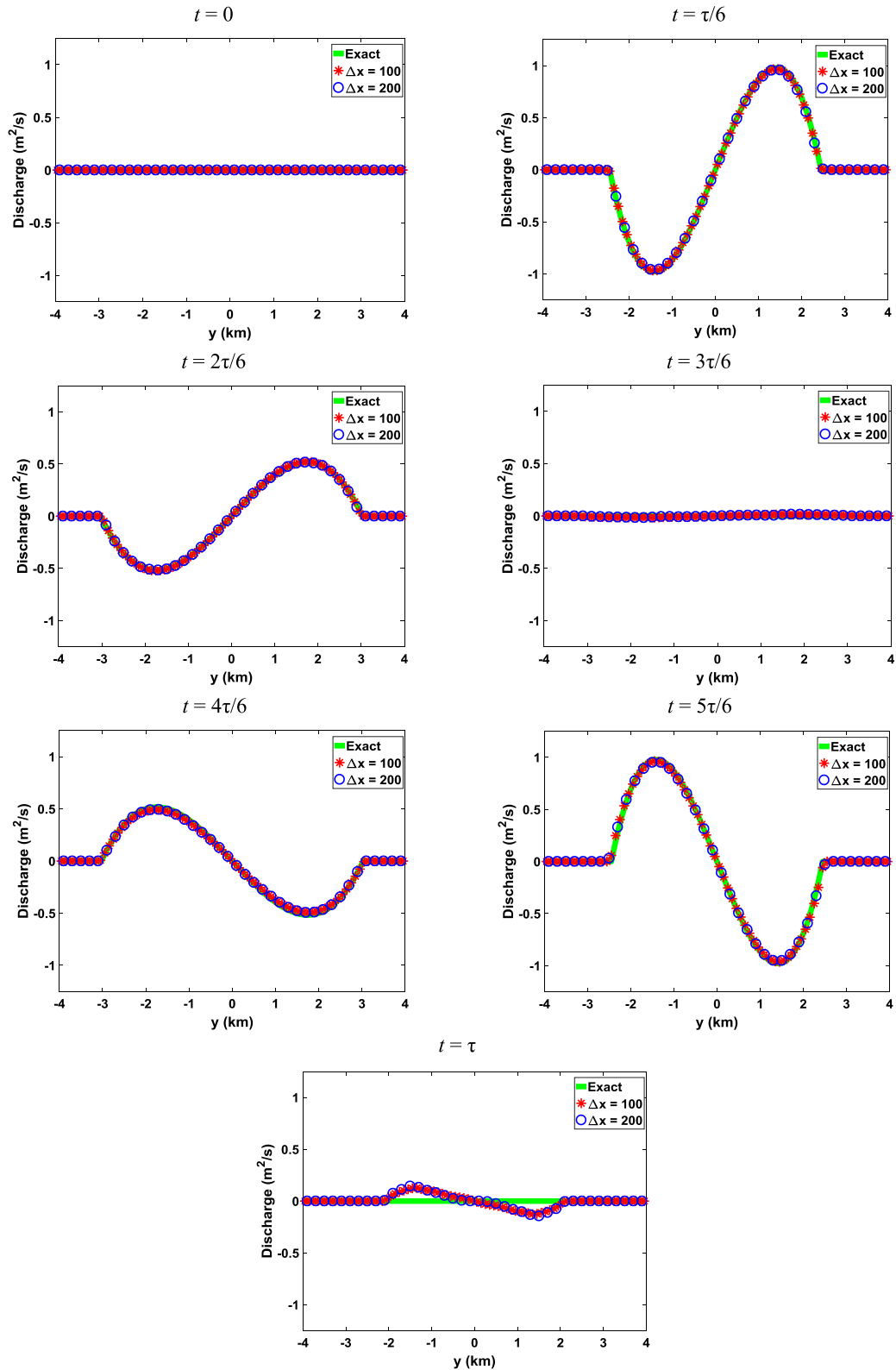
Fig. 14. Discharges sliced along $x = 0$ at six output times considering two mesh resolutions with cell size $\Delta x = 100$ and 200.

Table 2a
L^1-norm, L^2-norm and L^∞-norm errors and orders of accuracy for the 2D parabolic bowl test: analysis for the water depth variable, h, at $t = \tau/2$.

Δx	L^1-error	L^1-order	L^2-error	L^2-order	L^∞-error	L^∞-order
400.0	$4.60\mathrm{E}^{-03}$	–	$4.70\mathrm{E}^{-03}$	–	$5.80\mathrm{E}^{-03}$	–
200.0	$1.10\mathrm{E}^{-03}$	2.031	$1.20\mathrm{E}^{-03}$	2.000	$1.40\mathrm{E}^{-03}$	2.014
100.0	$2.77\mathrm{E}^{-04}$	2.021	$2.92\mathrm{E}^{-04}$	2.011	$4.33\mathrm{E}^{-04}$	1.740
50.0	$6.70\mathrm{E}^{-05}$	2.048	$7.08\mathrm{E}^{-05}$	2.044	$1.02\mathrm{E}^{-04}$	2.085
25.0	$1.56\mathrm{E}^{-05}$	2.100	$1.67\mathrm{E}^{-05}$	2.085	$3.80\mathrm{E}^{-05}$	1.426
12.5	$3.39\mathrm{E}^{-06}$	2.207	$3.82\mathrm{E}^{-06}$	2.129	$1.32\mathrm{E}^{-05}$	1.522

Table 2b
L^1-norm, L^2-norm and L^∞-norm errors and orders of accuracy for the 2D parabolic bowl test: analysis for y-direction discharge, q_y, at $t = \tau/2$.

Δx	L^1-error	L^1-order	L^2-error	L^2-order	L^∞-error	L^∞-order
400.0	$3.76\mathrm{E}^{-02}$	–	$4.58\mathrm{E}^{-02}$	–	$7.42\mathrm{E}^{-02}$	–
200.0	$7.30\mathrm{E}^{-03}$	2.372	$8.20\mathrm{E}^{-03}$	2.484	$1.36\mathrm{E}^{-02}$	2.447
100.0	$1.60\mathrm{E}^{-03}$	2.215	$1.70\mathrm{E}^{-03}$	2.266	$3.10\mathrm{E}^{-03}$	2.138
50.0	$1.89\mathrm{E}^{-04}$	3.052	$2.25\mathrm{E}^{-04}$	2.919	$4.70\mathrm{E}^{-04}$	2.718
25.0	$7.47\mathrm{E}^{-05}$	1.338	$8.97\mathrm{E}^{-05}$	1.326	$2.37\mathrm{E}^{-04}$	0.986
12.5	$4.18\mathrm{E}^{-05}$	0.837	$5.06\mathrm{E}^{-05}$	0.827	$1.11\mathrm{E}^{-04}$	1.096

Table 3a
L^1-norm, L^2-norm and L^∞-norm errors and orders of accuracy for the 2D parabolic bowl test: analysis for the water depth variable, h, at $t = \tau$.

Δx	L^1-error	L^1-order	L^2-error	L^2-order	L^∞-error	L^∞-order
400.0	$7.30\mathrm{E}^{-03}$	–	$7.03\mathrm{E}^{-03}$	–	$9.40\mathrm{E}^{-03}$	–
200.0	$1.80\mathrm{E}^{-03}$	2.022	$1.80\mathrm{E}^{-03}$	2.009	$2.30\mathrm{E}^{-03}$	2.009
100.0	$4.39\mathrm{E}^{-04}$	2.029	$4.59\mathrm{E}^{-04}$	1.982	$5.93\mathrm{E}^{-04}$	1.978
50.0	$1.07\mathrm{E}^{-04}$	2.035	$1.12\mathrm{E}^{-04}$	2.039	$1.50\mathrm{E}^{-04}$	1.988
25.0	$2.69\mathrm{E}^{-05}$	1.995	$2.70\mathrm{E}^{-05}$	2.048	$3.68\mathrm{E}^{-05}$	2.024
12.5	$7.69\mathrm{E}^{-06}$	1.806	$7.00\mathrm{E}^{-06}$	1.947	$9.51\mathrm{E}^{-06}$	1.951

Table 3b
L^1-norm, L^2-norm and L^∞-norm errors and orders of accuracy for the 2D parabolic bowl test: analysis for y-direction discharge, q_y, at $t = \tau$.

Δx	L^1-error	L^1-order	L^2-error	L^2-order	L^∞-error	L^∞-order
400.0	$3.44\mathrm{E}^{-02}$		$3.60\mathrm{E}^{-02}$	–	$4.58\mathrm{E}^{-02}$	–
200.0	$8.90\mathrm{E}^{-03}$	1.951	$9.40\mathrm{E}^{-03}$	1.929	$1.27\mathrm{E}^{-02}$	1.855
100.0	$2.40\mathrm{E}^{-03}$	1.901	$2.60\mathrm{E}^{-03}$	1.860	$3.80\mathrm{E}^{-03}$	1.717
50.0	$6.90\mathrm{E}^{-04}$	1.787	$8.00\mathrm{E}^{-04}$	1.702	$1.30\mathrm{E}^{-03}$	1.621
25.0	$2.65\mathrm{E}^{-04}$	1.382	$3.24\mathrm{E}^{-04}$	1.302	$4.67\mathrm{E}^{-04}$	1.424
12.5	$1.03\mathrm{E}^{-04}$	1.366	$1.34\mathrm{E}^{-04}$	1.276	$2.04\mathrm{E}^{-04}$	1.191

Furthermore, a mesh convergence analysis (as in Section 3.1.1) is achieved, considering L^1-, L^2- and L^∞-errors and their relative orders for the sliced profiles of the depth and discharge (in Figs. 13 and 14) on six meshes (i.e. with grid spacing $\Delta x = \Delta y = 12.5, 25, 50, 100, 200$ and 400, respectively). The analysis is done at the times $t = \tau/2$ and τ, which represent a wetting stage and a drying stage, respectively. Results of this analysis are presented in Tables 2 and 3.

For the water depth variable, as shown in Tables 2a and 3a, the acquired orders-of-accuracy are consistently very close to second-order for all the meshes considering L^1- and L^2-orders. Though a drop in the L^∞-orders (to around 1.5) is noticed at $t = \tau/2$ (Table 2a) on the finest meshes, L^∞-orders at $t = \tau$ (Table 3a) remain consistently second-order. For the y-direction discharge variable, the results in Tables 2b and 3b show alternating orders-of-accuracy in the range of 0.8–3.0 at $t = \tau/2$ (Table 2b), and of 1.2–2.0 at $t = \tau$ (Table 2b). Excluding the results associated with two finest meshes in Tables 2b and 3b, all L^1-, L^2- and L^∞-orders indicate second-order accurate predictions for the discharge variable. Arguably, the drop in L^1-, L^2- and L^∞-orders for the two finest meshes, together with their alternating character on the coarser meshes, are most likely caused by the aforementioned deficiency in capturing the zero discharges occurring at $t = \tau/2$ and $t = \tau$ (see Fig. 14). Nonetheless, these results reveal that the proposed slope-decoupled DG2 solver has a good tendency to deliver second-order accurate simulations of fully 2D nonlinear shallow
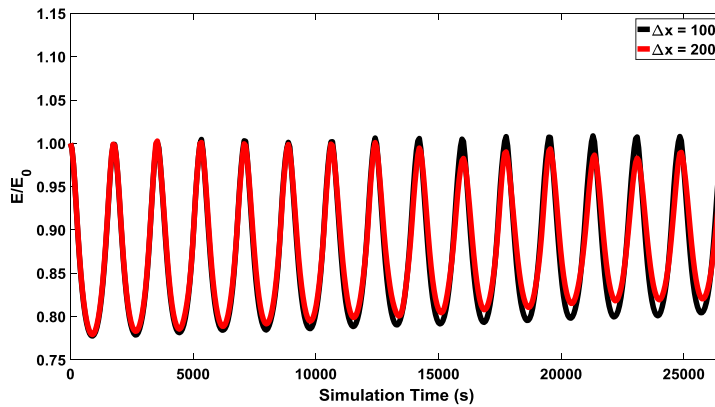
Fig. 15. Time evolution of the domain-integrated total energy (up to $t = 15\tau$).

water flows over uneven topography with constant wetting and drying, in addition to being formally a second-order accurate scheme as shown in the previous analysis in Table 1 (Section 3.1.1).

Finally, we assess the ability of the current scheme to conserve the energy property, as quantified by the following domain-integrated total energy over time, via Eq. (123):

$$E\left(t\right) = \int_{-4000}^{+4000} \left(\frac{1}{2}hu^2 + \frac{1}{2}g(h+z)^2\right)dx \tag{123}$$

The equation is evaluated up to $t = 15\tau$, which represents a long time evolution. Simulations are run considering two meshes with cell spacing $\Delta x = \Delta y = 100$ m and 200 m, consistent with the results in Figs. 13 and 14. Over each mesh, the total energy $E\left(t\right)$ is calculated over time and then normalised by the initial energy $E_0 = E(0)$. Fig. 15 displays the time evolution of the normalised energy for each of the two meshes. Generally, a consistent (alternating) variation in the normalised energy evolution is observed, which is expected as the kinetic energy drops to zero every time the velocity vanishes due to the switch between wetting and drying. With the coarser mesh, the amplitudes of the energy appear to reduce faster with time, especially at the highest peaks than with the finer mesh. Since the attenuation effect on the energy is clearly affected by the mesh size, refining the mesh is likely to improve the results. Regardless, there is no significant energy loss throughout the simulation, which confirms that the entirely slope-decoupled DG2 scheme is satisfactorily energy conservative.

4. Summary and conclusions

In this work, we have presented the conceptual formulation of a second-order Discontinuous Galerkin (DG2) numerical solver of the 2D depth-averaged Shallow Water Equations (SWE) on quadrilateral elements. The derivation of the proposed DG2-SWE solver considered the *standard form* (i.e. based on the stencil in Fig. 1) as a starting point, which was then simplified to produce the so-called *slope-decoupled form* (i.e. based on the stencil in Fig. 2). In the slope-decoupled DG2 form, theoretical complexity was deliberately compromised to acquire a setting whereby key challenges relevant to the practical modelling of hydrodynamics are conveniently addressable (i.e. well-balancing between spatial flux and steep topography gradients, robust incorporation of wetting and drying processes, and reduction of operational costs). The well-balanced property of the slope-decoupled DG2 scheme was thoroughly studied for two possible approaches to discretise the bed slope terms, i.e. in a consistent manner based on the local DG2 discrete planar projection to the topography. The first approach, via Eqs. (83) and (84), involves both x- and y-directional bed slope coefficients, i.e. as full contribution for the planar topography projections. In the second approach, via Eqs. (85) and (86), any possible cross-dimensional bed slope dependency was zeroed to keep consistent with the slope-decoupled hypothesis adopted for the simplified 2D-DG2-SWE solver. It was theoretically demonstrated that this solver can only be *partially* well-balanced (i.e. for the means and *some* slope coefficients) with the first approach for integrating DG2 topography projections. In contrast, when complemented with the second approach, the slope-decoupled 2D-DG2-SWE solver is *fully* well-balanced (i.e. for *all* the coefficients spanning DG2

solutions). Selected numerical tests were employed to verify the applicability of the slope-decoupled DG2 scheme, considering performance comparisons with the standard DG2 scheme, and verifications of its conservative abilities relating to 2D modelling of hydrodynamics.

The performance comparisons indicated that the slope-decoupled DG2 scheme is able to achieve second-order mesh convergence and similar predictive capability as the standard DG2 scheme. Further numerical verifications revealed a *fully* well-balanced behaviour of the aforementioned slope-decoupled DG2 scheme (i.e. combined with the second approach for the DG2 integration of bed slope coefficients), even when the topography admits non-differentiable shapes (e.g. building like) and/or when the domain is partially dry (e.g. when the local planar DG2 flow solution cut through the local planar topography projection). Moreover, the scheme could acheive second-order mesh convergence when the flow involved moving wet–dry fronts over an uneven topography, and shows a remarkable capability in simulating realistic features associated with 2D modelling of hydrodynamics (i.e. wetting and drying processes, flow over irregular terrain, flow curvatures, energy conservation). It can therefore be concluded that the slope-decoupled DG2 scheme is a valid option to formulate a flood model with desirable robustness properties of relevance to simulate real-world applications.

Acknowledgements

References

[1] A. Duran, F. Marche, Recent advances on the discontinuous Galerkin method for shallow water equations with topography source terms, Comput. & Fluids 101 (2014) 88–104.
[2] Y. Xing, C.W. Shu, A survey of high order schemes for the shallow water equations, J. Math. Study 47 (3) (2014) 221–249.
[3] C.T. Miller, et al., Numerical simulation of water resources problems: Models, methods, and trends, Adv. Water Resour. 51 (2013) 405–437.
[4] C.-W. Shu, High order WENO and DG methods for time-dependent convection-dominated PDEs: A brief survey of several recent developments, J. Comput. Phys. 316 (2016) 598–613.
[5] C. Paniconi, M. Putti, Physically based modeling in catchment hydrology at 50: Survey and outlook, Water Resour. Res. 51 (9) (2015) 7090–7129.
[6] N. Wintermeyer, et al., An entropy stable nodal discontinuous Galerkin method for the two dimensional shallow water equations on unstructured curvilinear meshes with discontinuous bathymetry, J. Comput. Phys. 340 (2017) 200–242.
[7] S. Godunov, A difference method for numerical calculation of discontinuous solutions of the equations of hydrodynamics, Mat. Sb. 47 (3) (1959) 271–306.
[8] V. Guinot (Ed.), Godunov-Type Schemes: An Introduction for Engineers, Elsevier, Amsterdam, 2003.
[9] E.F. Toro, P. Garcia-Navarro, Godunov-type methods for free-surface shallow flows: A review, J. Hydraul. Res. 45 (6) (2007) 736–751.
[10] E.F. Toro, Riemann Solvers and Numerical Methods for Fluid Dynamics: A Practical Introduction, Springer-Verlag, Berlin Heidelberg, 1999.
[11] E.F. Toro (Ed.), Shock-Capturing Methods for Free-Surface Shallow Flows, John Wiley & Sons, Ltd, 2001.
[12] J. Jaśkowiec, Very high order discontinuous Galerkin method in elliptic problems, Comput. Mech. (2017).
[13] R. Biswas, K.D. Devine, J.E. Flaherty, Parallel, adaptive finite element methods for conservation laws, Appl. Numer. Math. 14 (1) (1994) 255–283.
[14] C. Eskilsson, et al., A parallel high-order discontinuous galerkin shallow water model, in: G. Allen, et al. (Eds.), Computational Science–ICCS 2009, Springer Berlin Heidelberg, 2009, pp. 63–72.
[15] S.R. Brus, et al., Performance and scalability improvements for discontinuous galerkin solutions to conservation laws on unstructured grids, J. Sci. Comput. 70 (1) (2017) 210–242.
[16] C. Dawson, et al., A parallel local timestepping Runge–Kutta discontinuous Galerkin method with applications to coastal ocean modeling, Comput. Methods Appl. Mech. Engrg. 259 (2013) 154–165.
[17] A. Samii, C. Michoski, C. Dawson, A parallel and adaptive hybridized discontinuous Galerkin method for anisotropic nonhomogeneous diffusion, Comput. Methods Appl. Mech. Engrg. 304 (2016) 118–139.
[18] M. Fuhry, A. Giuliani, L. Krivodonova, Discontinuous Galerkin methods on graphics processing units for nonlinear hyperbolic conservation laws, Internat. J. Numer. Methods Fluids 76 (12) (2014) 982–1003.
[19] A. Klöckner, et al., Nodal discontinuous Galerkin methods on graphics processors, J. Comput. Phys. 228 (21) (2009) 7863–7882.
[20] M. DuChene, et al., A framework for running the ADCIRC discontinuous galerkin storm surge model on a GPU, Procedia Comput. Sci. 4 (2011) 2017–2026.
[21] J. Chan, et al., GPU-accelerated discontinuous Galerkin methods on hybrid meshes, J. Comput. Phys. 318 (2016) 142–168.
[22] C.J. Conroy, E.J. Kubatko, hp discontinuous Galerkin methods for the vertical extent of the water column in coastal settings part I: Barotropic forcing, J. Comput. Phys. 305 (2016) 1147–1171.

[23] C. Eskilsson, An hp-adaptive discontinuous Galerkin method for shallow water flows, Internat. J. Numer. Methods Fluids 67 (11) (2011) 1605–1623.

[24] C. Eskilsson, S.J. Sherwin, A triangular spectral/hp discontinuous Galerkin method for modelling 2D shallow water equations, Internat. J. Numer. Methods Fluids 45 (6) (2004) 605–623.

[25] E.J. Kubatko, J.J. Westerink, C. Dawson, hp Discontinuous Galerkin methods for advection dominated problems in shallow water flow, Comput. Methods Appl. Mech. Engrg. 196 (1–3) (2006) 437–451.

[26] E.J. Kubatko, et al., Dynamic p-adaptive Runge–Kutta discontinuous Galerkin methods for the shallow water equations, Comput. Methods Appl. Mech. Engrg. 198 (21–26) (2009) 1766–1774.

[27] B. Seny, et al., Multirate time stepping for accelerating explicit discontinuous Galerkin computations with application to geophysical flows, Internat. J. Numer. Methods Fluids 71 (1) (2013) 41–64.

[28] C.J. Trahan, C. Dawson, Local time-stepping in Runge–Kutta discontinuous Galerkin finite element methods applied to the shallow-water equations, Comput. Methods Appl. Mech. Engrg. 217–220 (2012) 139–152.

[29] J.-F. Remacle, et al., An adaptive discretization of shallow-water equations based on discontinuous Galerkin methods, Internat. J. Numer. Methods Fluids 52 (8) (2006) 903–923.

[30] N. Gerhard, et al., Multiwavelet-based grid adaptation with discontinuous Galerkin schemes for shallow water equations, J. Comput. Phys. 301 (2015) 265–288.

[31] G. Kesserwani, et al., Multiwavelet discontinuous Galerkin h-adaptive shallow water model, Comput. Methods Appl. Mech. Engrg. 294 (2015) 56–71.

[32] G. Kesserwani, Q. Liang, RKDG2 shallow-water solver on non-uniform grids with local time steps: Application to 1D and 2D hydrodynamics, Appl. Math. Model. 39 (3–4) (2015) 1317–1340.

[33] C. Dawson, S. Sun, M.F. Wheeler, Compatible algorithms for coupled flow and transport, Comput. Methods Appl. Mech. Engrg. 193 (23) (2004) 2565–2580.

[34] G. Kesserwani, A. Shamkhalchian, M. Zadeh, Fully coupled discontinuous galerkin modeling of dam-break flows over movable bed with sediment transport, J. Hydraul. Eng. 140 (4) (2014) 06014006.

[35] V. Vallaeys, et al., Discontinuous Galerkin modeling of the Columbia River's coupled estuary-plume dynamics, Ocean Modell. (2018).

[36] D.W. West, et al., A multidimensional discontinuous Galerkin modeling framework for overland flow and channel routing, Adv. Water Resour. 102 (2017) 142–160.

[37] M. Zhang, C.W. Shu, An analysis of and a comparison between the discontinuous Galerkin and the spectral finite volume methods, Comput. & Fluids 34 (4–5) (2003) 581–592.

[38] T. Zhou, Y. Li, C.W. Shu, Numerical comparison of WENO finite volume and Runge–Kutta discontinuous Galerkin methods, J. Sci. Comput. 16 (2) (2001) 145–171.

[39] E. Kubatko, et al., A performance comparison of continuous and discontinuous finite element shallow water models, J. Sci. Comput. 40 (1–3) (2009) 315–339.

[40] G. Kesserwani, Topography discretization techniques for Godunov-type shallow water numerical models: a comparative study, J. Hydraul. Res. 51 (4) (2013) 351–367.

[41] G. Kesserwani, Y. Wang, Discontinuous Galerkin flood model formulation: Luxury or necessity? Water Resour. Res. 50 (8) (2014) 6522–6541.

[42] L. Minatti, P.N. De Cicco, L. Solari, Second order discontinuous Galerkin scheme for compound natural channels with movable bed. Applications for the computation of rating curves, Adv. Water Resour. 93 (2016) 89–104.

[43] S. Marras, et al., A residual-based shock capturing scheme for the continuous/discontinuous spectral element solution of the 2D shallow water equations, Adv. Water Resour. 114 (2018) 45–63.

[44] M.J. Vuik, J.K. Ryan, Multiwavelet troubled-cell indicator for discontinuity detection of discontinuous Galerkin schemes, J. Comput. Phys. 270 (2014) 138–160.

[45] M. Vuik, J. Ryan, Automated parameters for troubled-cell indicators using outlier detection, SIAM J. Sci. Comput. 38 (1) (2016) A84–A104.

[46] A. Burbeau, P. Sagaut, C.H. Bruneau, A problem-independent limiter for high-order Runge–Kutta discontinuous Galerkin methods, J. Comput. Phys. 169 (1) (2001) 111–150.

[47] J. Qiu, C.W. Shu, A comparison of troubled-cell indicators for Runge–Kutta Discontinuous Galerkin methods using weighted essentially nonoscillatory limiters, SIAM J. Sci. Comput. 27 (3) (2005) 995–1013.

[48] J.X. Qiu, C.W. Shu, Runge–Kutta discontinuous Galerkin method using WENO limiters, SIAM J. Sci. Comput. 26 (3) (2005) 907–929.

[49] L. Krivodonova, Limiters for high-order discontinuous Galerkin methods, J. Comput. Phys. 226 (1) (2007) 879–896.

[50] M. Yang, Z.J. Wang, A parameter-free generalized moment limiter for high-order methods on unstructured grids, Adv. Appl. Math. Mech. 1 (4) (2009) 451–480.

[51] X. Zhong, C.-W. Shu, A simple weighted essentially nonoscillatory limiter for Runge–Kutta discontinuous Galerkin methods, J. Comput. Phys. 232 (1) (2013) 397–415.

[52] C. Michoski, et al., Adaptive hierarchic transformations for dynamically p-enriched slope-limiting over discontinuous Galerkin systems of generalized equations, J. Comput. Phys. 230 (22) (2011) 8028–8056.

[53] L. Krivodonova, et al., Shock detection and limiting with discontinuous Galerkin methods for hyperbolic conservation laws, Appl. Numer. Math. 48 (3–4) (2004) 323–338.

[54] B. Sanders, S. Bradford, Impact of limiters on accuracy of high-resolution flow and transport models, J. Eng. Mech. 132 (1) (2006) 87–98.

[55] P. Mocz, et al., A discontinuous Galerkin method for solving the fluid and MHD equations in astrophysical simulations, Mon. Not. R. Astron. Soc. 437 (2014) 397–414.

[56] H. An, S. Yu, An accurate multidimensional limiter on quadtree grids for shallow water flow simulation, J. Hydraul. Res. 52 (4) (2014) 565–574.

[57] S. Vater, N. Beisiegel, J. Behrens, A limiter-based well-balanced discontinuous Galerkin method for shallow-water flows with wetting and drying: One-dimensional case, Adv. Water Resour. 85 (2015) 1–13.

[58] D. Zhang, et al., A review on TVD schemes and a refined flux-limiter for steady-state calculations, J. Comput. Phys. 302 (C) (2015) 114–154.

[59] C. Michoski, et al., A comparison of artificial viscosity, limiters, and filters, for high order discontinuous galerkin solutions in nonlinear settings, J. Sci. Comput. 66 (1) (2015) 406–434.

[60] G. Kesserwani, Q. Liang, A conservative high-order discontinuous Galerkin method for the shallow water equations with arbitrary topography, Internat. J. Numer. Methods Engrg. 86 (1) (2011) 47–69.

[61] G. Kesserwani, Q. Liang, Influence of total-variation-diminishing slope limiting on local discontinuous Galerkin solutions of the shallow water equations, J. Hydraul. Eng. 138 (2) (2012) 216–222.

[62] V. Caleffi, A. Valiani, G. Li, A comparison between bottom-discontinuity numerical treatments in the DG framework, Appl. Math. Model. 40 (17–18) (2016) 7516–7531.

[63] D. Caviedes-Voullième, G. Kesserwani, Benchmarking a multiresolution discontinuous Galerkin shallow water model: Implications for computational hydraulics, Adv. Water Resour. 86 (Part A) (2015) 14–31.

[64] A. Ern, S. Piperno, K. Djadel, A well-balanced Runge–Kutta discontinuous Galerkin method for the shallow-water equations with flooding and drying, Internat. J. Numer. Methods Fluids 58 (1) (2008) 1–25.

[65] S. Bunya, et al., A wetting and drying treatment for the Runge–Kutta discontinuous Galerkin solution to the shallow water equations, Comput. Methods Appl. Mech. Engrg. 198 (17–20) (2009) 1548–1562.

[66] O. Gourgue, et al., A flux-limiting wetting–drying method for finite-element shallow-water models, with application to the Scheldt Estuary, Adv. Water Resour. 32 (12) (2009) 1726–1739.

[67] T. Kärnä, et al., A fully implicit wetting–drying method for DG-FEM shallow water models, with an application to the Scheldt Estuary, Comput. Methods Appl. Mech. Engrg. 200 (5–8) (2011) 509–524.

[68] Y. Xing, X. Zhang, Positivity-preserving well-balanced discontinuous Galerkin methods for the shallow water equations on unstructured triangular meshes, J. Sci. Comput. 57 (1) (2013) 19–41.

[69] P. Brufau, P. García-Navarro, M.E. Vázquez-Cendón, Zero mass error using unsteady wetting-drying conditions in shallow flows over dry irregular topography, Internat. J. Numer. Methods Fluids 45 (10) (2004) 1047–1082.

[70] E. Audusse, M.-O. Bristeau, A well-balanced positivity preserving "second-order" scheme for shallow water flows on unstructured meshes, J. Comput. Phys. 206 (1) (2005) 311–333.

[71] Q. Liang, F. Marche, Numerical resolution of well-balanced shallow water equations with complex source terms, Adv. Water Resour. 32 (6) (2009) 873–884.

[72] G. Kesserwani, Q. Liang, A discontinuous Galerkin algorithm for the two-dimensional shallow water equations, Comput. Methods Appl. Mech. Engrg. 199 (49–52) (2010) 3356–3368.

[73] G. Kesserwani, Q. Liang, Dynamically adaptive grid based discontinuous Galerkin shallow water model, Adv. Water Resour. 37 (2012) 23–39.

[74] D. Wirasaet, et al., Discontinuous Galerkin methods with nodal and hybrid modal/nodal triangular, quadrilateral, and polygonal elements for nonlinear shallow water flow, Comput. Methods Appl. Mech. Engrg. 270 (2014) 113–149.

[75] D. Wirasaet, et al., A performance comparison of nodal discontinuous Galerkin methods on triangles and quadrilaterals, Internat. J. Numer. Methods Fluids 64 (10–12) (2010) 1336–1362.

[76] X. Lu, S. Xie, Conventional versus pre-balanced forms of the shallow-water equations solved using finite-volume method, Ocean Modell. 101 (2016) 113–120.

[77] P.L. Roe, Approximate Riemann solvers, parameter vectors, and difference schemes, J. Comput. Phys. 43 (2) (1981) 357–372.

[78] G. Kesserwani, et al., Well-balancing issues related to the RKDG2 scheme for the shallow water equations, Internat. J. Numer. Methods Fluids 62 (4) (2010) 428–448.

[79] G. Kesserwani, Q. Liang, Locally limited and fully conserved RKDG2 shallow water solutions with wetting and drying, J. Sci. Comput. 50 (1) (2012) 120–144.

[80] W. Thacker, Some exact solutions to the nonlinear shallow-water wave equations, J. Fluid Mech. 107 (1981) 499–508.